Photochemistry and Photobiology, 2011, 87: 199–207

Photosensitization Reaction-Induced Acute Electrophysiological Cell Response of Rat Myocardial Cells in Short Loading Periods of Talaporfin Sodium or Porfimer Sodium

Arisa Ito*[1], Takehiro Kimura[2], Shunichiro Miyoshi[2], Satoshi Ogawa[3] and Tsunenori Arai[1]

[1]School of Fundamental Science and Technology, Graduate School of Science and Technology, Keio University, Kohoku-ku, Yokohama, Japan
[2]Cardiopulmonary Division, Department of Internal Medicine, Keio University School of Medicine, Shinjuku-ku, Tokyo, Japan
[3]Mita Hospital, International University of Health and Welfare, Minato-ku, Tokyo, Japan

Received 8 August 2010, accepted 20 October 2010, DOI: 10.1111/j.1751-1097.2010.00846.x

ABSTRACT

Electrophysiological responses of rat myocardial cells to exogenous photosensitization reactions for a short period of incubation with two photosensitizers, talaporfin sodium or porfimer sodium, were measured in a subsecond time scale. The loading period of the photosensitizer when the photosensitizer might not be taken up by the cells was selected as 15 min, which was determined by the fluorescence microscopic observation. We measured the intracellular Ca^{2+} concentration ($[Ca^{2+}]_{in}$) by using a fluorescent Ca^{2+} indicator, Fluo-4 AM, under a high-speed confocal laser microscope to evaluate the acute electrophysiological cell response to the photosensitization reaction. The measured temporal change in Fluo-4 fluorescence intensity indicated that the response to the photosensitization reaction might be divided into two phases in both photosensitizers. The first phase is acute response: disappearance of Ca^{2+} oscillation when irradiation starts, which might be caused by ion channel dysfunction. The second phase is slow response: $[Ca^{2+}]_{in}$ elevation indicating influx of Ca^{2+} due to the concentration gradient. The continuous Ca^{2+} influx followed by changes in cell morphology suggested micropore formation on the surface of the cell membrane, resulting in necrotic cell death.

INTRODUCTION

Photosensitization reaction-induced cellular damage has been widely applied to clinical therapies such as noninvasive cancer therapy and age-related macular degeneration (1,2). Photochemical interactions involve photons, photosensitizers and oxygen generate reactive oxygen species, mainly singlet molecular oxygen (3–5). The activated singlet oxygen reacts with many biological molecules, including lipids, proteins and nucleic acids, resulting in apoptotic or necrotic cellular damage (6–8). The cellular response to photosensitization reaction is dependent on photosensitizer distribution, which is determined by the loading process and the physicochemical properties of the photosensitizer molecule, particularly molecular size, structure, charge and water solubility (9,10). The photosensitization reaction may cause selective organelle damage when the photosensitizer localizes to certain cellular compartments such as the mitochondria or lysosomes after a long incubation period (4,6). These damages to organelles may initiate enzyme activation followed by apoptosis. After a short incubation period of several minutes, the photosensitizer may not be taken up into the cells and may be distributed on the cell membrane or outside the cells (5). The membrane-bound photosensitizers irradiated by excitation light may induce membrane disruption, for example, due to micropore formation and ion channel dysfunction, resulting in morphological and electrophysiological changes in the cells (6,11).

Oxidative injury is known to be induced by exposure of cells to exogenous photosensitization reactions that increase intracellular free Ca^{2+} concentrations ($[Ca^{2+}]_{in}$) (12–14). The importance of Ca^{2+} for the viability and electrophysiological function of cells is well recognized (15,16). Ca^{2+} overload may play a role in photosensitization reaction-induced necrotic cell death (6). The intracellular Ca^{2+} dynamics during photosensitization reaction has been studied in various cell types such as erythrocytes (17), cardiomyocytes (18,19) and cancer cells (13,20). However, to our knowledge, there are no reports on the acute effect of exogenous photosensitization reactions on $[Ca^{2+}]_{in}$ in myocardial cells as observed in the subsecond scale.

In this study, we focused on the early events of Ca^{2+} dynamics during the onset of exogenous photosensitization reaction in short period of photosensitizer incubation. The photosensitization reaction was induced by short-time incubation of rat myocardial cells with two distinctive clinically approved photosensitizers, porfimer sodium and talaporfin sodium. Porfimer sodium (Photofrin®), a preparation of hematoporphyrin derivatives (HPD), is the most popular photosensitizer and has been applied to various therapies for malignant tumors (1,21). The lipophilic character of porfimer sodium may cause it to localize in the cell membrane and in the subcellular membrane. The cellular uptake of this photosensitizer has been studied in various types of tumor cells. Its subcellular pharmacokinetics in tumor cells is as follows:

*Corresponding author email: arisa.i@arai.appi.keio.ac.jp (Arisa Ito)

distribution on the cell membrane in the first several tens of minutes of incubation, slow uptake into the cells and then localization to other organelle membranes, especially the mitochondria, lysosome and Golgi apparatus in the final stage (22). The other photosensitizer used was the hydrophilic chlorin photosensitizer talaporfin sodium, also called mono-L-aspartyl chlorin e6 (NPe6), a chlorophyll derivative (1,23). Talaporfin sodium has been approved for early-stage lung cancer therapy in Japan as Laserphyrin® (24,25). Talaporfin sodium has been reported to localize to lysosomes after a long period of incubation (26–28). The change in intracellular Ca^{2+} concentration was measured using a high-speed confocal microscope with a frame rate of five frames per second to assess the electrophysiological cellular responses to photosensitization reactions with talaporfin sodium and porfimer sodium.

MATERIALS AND METHODS

Cell culture. Rat myocardial cells (Primary Cell Co., Ltd., Hokkaido, Japan) were cultured in Medium I (Dulbecco's modified Eagle's medium/nutrient mixture F-12 [D-MEM/F-12] supplemented with 10% fetal bovine serum, 100 U mL^{-1} penicillin and 100 μg mL^{-1} streptomycin; all from Invitrogen, Carlsbad, CA) in an atmosphere of 95% air and 5% CO_2 at 37°C.

Photosensitizers. The photosensitization reaction was performed using two kinds of photosensitizers, a hydrophilic photosensitizer (talaporfin sodium) and a lipophilic photosensitizer (porfimer sodium). Talaporfin sodium (Meiji Seika Kaisha Ltd., Tokyo, Japan), 799.69 MW, has a major absorption peak of the Q band at 664 nm and an average molar absorbance of 2.7×10^4 M^{-1} cm^{-1} at 667 nm in a medium (without phenol red) containing 10% fetal bovine serum (29). Porfimer sodium (Wyeth Lederle, Japan Ltd., Tokyo, Japan), 1,231.28–4,883.30 MW, has a major absorption peak of Q band at 625 nm and an average molar absorbance of 2.9×10^3 M^{-1} cm^{-1} at 630 nm in the same mixture as mentioned above (29).

Photocytotoxic effect. The isolated rat myocardial cells were placed in collagen-coated 96 well microplates at a concentration of 2×10^4 cells per well and cultured in Medium I at 37°C in 5% CO_2. After 6–7 days in culture, the cells were loaded with 10–50 μg mL^{-1} talaporfin sodium or porfimer sodium medium solution and kept in the dark for 30 min. After incubation in the dark, the cells were exposed to a 670 nm red diode laser (OpticalFuel; Sony Co., Ltd., Tokyo, Japan) for talaporfin sodium or 633 nm red diode laser (HPD 5215; Intense Ltd., NJ) for porfimer sodium at a fluence rate of 150 mW cm^{-2} and a total fluence of 1–10 J cm^{-2}. The cell lethality rate with the photosensitization reaction was measured using a water-soluble tetrazolium-8 (WST-8) assay kit (Cell Counting Kit-8; Doujinkagaku Co., Ltd., Kumamoto, Japan). After irradiation, the culture medium was replaced with a medium without the photosensitizer and 10 μL of WST-8 was added to the wells. After 2 h incubation, the absorbance of the reaction products at 450 nm was measured using a microplate absorbance reader (Sunrise™; Tecan Group Ltd., Maennedorf, Switzerland). The cell lethality rate was calculated as a percentage relative to the absorbance of living cells in the reference well without the photosensitization reaction. The absorbance of the complete viable cells (cell lethality rate of 0%) was defined as the difference between the absorbance of the cells with no irradiation without photosensitizer loading and that of the cells irradiated by 10 J cm^{-2} laser light after incubation with 50 μg mL^{-1} talaporfin sodium or porfimer sodium. The normalized ratios characterized by the above definitions were used to calculate the cell lethality rate.

Subcellular distribution. The isolated rat myocardial cells were grown on 15 mm glass coverslips placed in a 35 mm petri dish 3 days before the experiment. The culture medium was replaced with 30 μg mL^{-1} talaporfin sodium or porfimer sodium dissolved in Medium II (minimal essential medium supplemented with 10% fetal bovine serum; all from Invitrogen) and then the cells were further incubated for 15 min for 3 h in the dark. To determine the subcellular uptake of the two photosensitizers in rat myocardial cells, the cells incubated with the photosensitizers were stained with a lysosome probe (for talaporfin sodium) or mitochondria probe (for porfimer sodium), since it has been reported that talaporfin sodium localizes to the lysosome and porfimer sodium localizes to the mitochondrion after a long incubation period with tumor cells (10,22,30). After photosensitizer incubation, the cells were washed with the fresh medium without photosensitizer and loaded with a lysosome probe, 1 μM LysoTracker Green (Molecular Probes Inc., Eugene, OR), or mitochondria probe, 1 μg mL^{-1} Rhodamine 123 (Molecular Probes Inc.) for an additional 30 min at room temperature. After staining, the medium was replaced with a fresh medium and the cells were placed on the stage of an inverted fluorescence microscope (BX51WI; Olympus Co., Ltd., Tokyo, Japan) equipped with ×40 water immersion lens (LUMPlanFL40 × W; Olympus Co., Ltd). Talaporfin sodium or porfimer sodium was excited at 400 ± 10 nm in the Solet band of these photosensitizers, using a 100 W mercury lamp with a band-pass filter, and the fluorescence was detected with a 600 nm long-pass filter. LysoTracker Green or Rhodamine 123 was excited by green light with a 470–495 nm band-pass filter, whereas a 510–550 nm band-pass filter was used to detect fluorescence. No interference was observed between the photosensitizers and organelle probe in the wavelengths used. Fluorescence images for both photosensitizers were taken using a near-infrared cooled CCD camera (Rolera-XR; QImaging, Burnaby, Canada). Image analysis was performed using ImageJ 1.41 (National Institute of Health, Bethesda, MD).

Intracellular Ca^{2+} concentration during the photosensitization reaction. Myocardial cells were grown on 15 mm glass coverslips placed in a 35 mm Petri dish for 2 days and then the change in intracellular free Ca^{2+} concentration ($[Ca^{2+}]_{in}$) during the exogenous photosensitization reaction was examined using a fluorescent Ca^{2+} indicator, Fluo-4 AM (Molecular Probes Inc). Fluo-4, a type of Fluo-4 AM hydrolyzed by cellular esterases inside the cells, has an absorption peak at 494 nm and a fluorescence peak at 516 nm (31,32); thus, the measurement of Fluo-4 fluorescence will not affect the photosensitization reaction. To measure the cellular response to the exogenous photosensitization reaction, in $[Ca^{2+}]_{in}$, the cells were loaded with 5 μM Fluo-4 AM dissolved in Medium II to a 2.2 mM total Ca^{2+} concentration in the medium for 20 min at room temperature. The medium was then replaced with 30 μg mL^{-1} talaporfin sodium or porfimer sodium for an additional 15 min. In this loading condition of "short period of incubation," both talaporfin sodium and porfimer sodium may not be taken up into the cells. The reaction was observed under a fluorescence microscope to determine the subcellular photosensitizer localization. The amount of photosensitizer taken up into the cellular compartment in the 15 min loading period might be less than 1/10 of that in 30 min incubation for talaporfin sodium. Porfimer sodium has been reported to distribute on the cell membrane in less than 2 h of incubation (22). The cell response in the condition of "long period of photosensitizer incubation" was also measured to compare the cellular response between the loading periods of photosensitizer. A long loading period was determined to be 1 h for talaporfin sodium and 3 h for porfimer sodium. Figure 1 shows the experimental setup for the measurement of $[Ca^{2+}]_{in}$ in rat myocardial cells during the photosensitization reaction with talaporfin sodium or porfimer sodium. Fluo-4 in the myocardial cells was excited with an argon laser at 488 nm (800BL; National Laser Co., Salt Lake City, UT) and talaporfin sodium or porfimer sodium was excited at 655 ± 25 nm (103 mW cm^{-2}) or 625 ± 25 nm (117 mW cm^{-2}), respectively, using a 100 W mercury lamp with a band-pass filter. Fluo-4 fluorescence images were obtained with a confocal laser microscope system (CSU-X1; Yokogawa Electric Company, Tokyo, Japan) mounted on a differential interference microscope (BX51WI-FL-IRDIC; Olympus Co., Ltd) with ×40 water immersion lens. Fluo-4 fluorescence was detected at the 500–540 nm band-pass filter with an electron multiplication CCD camera (DU897; Andor Technology, Belfast, UK) with a frame rate of 200 ms per frame. The detected images were analyzed by the image software iQ Core (Andor Technology). The average Fluo-4 fluorescence intensity inside the cells was used to assess the changes in $[Ca^{2+}]_{in}$ in myocardial cells.

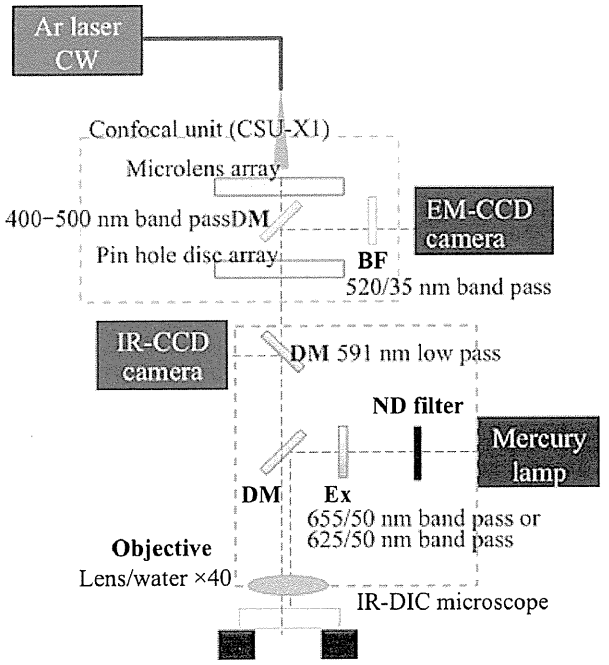

Figure 1. Experimental setup for the measurement of intracellular Ca^{2+} concentration in rat myocardial cells, using a high-speed confocal laser microscope during the photosensitization reaction with talaporfin sodium or porfimer sodium.

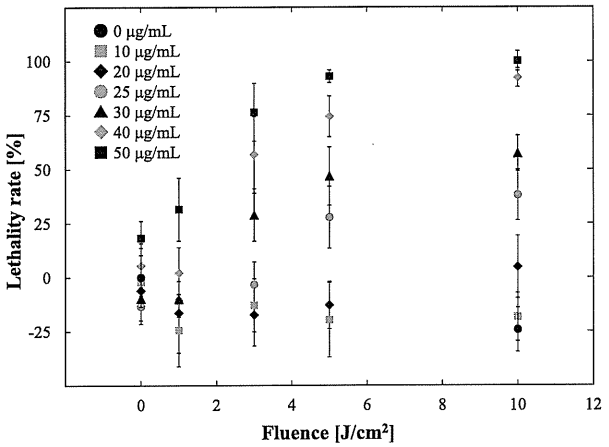

Figure 2. Cell lethality rate in the photosensitization reaction with talaporfin sodium was dependent on the fluence and photosensitizer concentration at the loading time of 30 min.

RESULTS

Photocytotoxic effect of photosensitization reaction with talaporfin sodium or porfimer sodium in rat myocardial cells

The examined parameters in the photosensitization reaction were photosensitizer concentration, laser light energy (in fluence, J cm^{-2}) and loading period. The variation in loading period induced little difference in photocytotoxicity. Figures 2 and 3 show the cell lethality change with fluence in various photosensitizer concentrations at the loading time of 30 min.

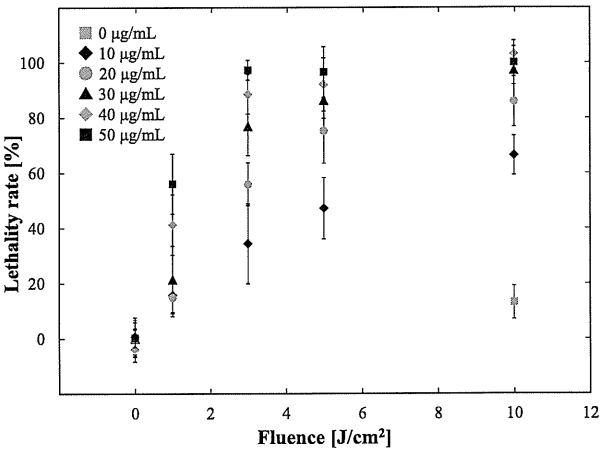

Figure 3. Cell lethality rate in the photosensitization reaction with porfimer sodium was dependent on the fluence and photosensitizer concentration at the loading time of 30 min.

The same tendency was observed in both photosensitizers; that is, the lethality rate increased with the increase in photosensitizer concentration and fluence. When the lethality rate was more than 50%, drastic morphological changes in cells were observed from the phase-contrast microscopic observation: first, a granulated cytoplasm, then bleb formation and finally cell shrinkage were seen. The photosensitizer concentration was selected as 30 μg mL^{-1} for the subsequent study based on the following requirements: more than 50% lethality rate at 10 J cm^{-2} and monotonous increase in lethality up to 10 J cm^{-2}.

Subcellular distribution of talaporfin sodium or porfimer sodium in rat myocardial cells

The subcellular distribution of talaporfin sodium and porfimer sodium in rat myocardial cells with the short loading period of up to 1 h in talaporfin sodium and 3 h in porfimer sodium was determined using a fluorescence microscope. The bright-field image, talaporfin sodium fluorescence image, LysoTracker Green fluorescence image and the merged image of talaporfin sodium fluorescence (red) and LysoTracker Green fluorescence (green) using the same myocardial cells at the incubation times of 15 min, 30 min and 45 min are shown in Fig. 4a–l. In the fluorescence image of Fig. 4b, the narrow distribution of talaporfin sodium, unlike the LysoTracker fluorescence distribution (Fig. 4d), indicates that talaporfin sodium might not be taken up into the cells in the 15 min loading period. When cells were incubated with talaporfin sodium for 30–45 min, the photosensitizer fluorescence distribution corresponded with the LysoTracker Green fluorescence distribution (Fig. 4h,l), which indicates that talaporfin sodium was taken up into the myocardial cells and localized to the lysosome over the 30 min incubation time.

The bright-field image, porfimer sodium fluorescence image, Rhodamine 123 fluorescence image and the merged image of porfimer sodium fluorescence (red) and Rhodamine 123 fluorescence (green) using the same myocardial cells in incubation times of 30 min, 2 h and 3 h are shown in Fig. 5a–l. In the case of 30 min incubation (Fig. 5b), the

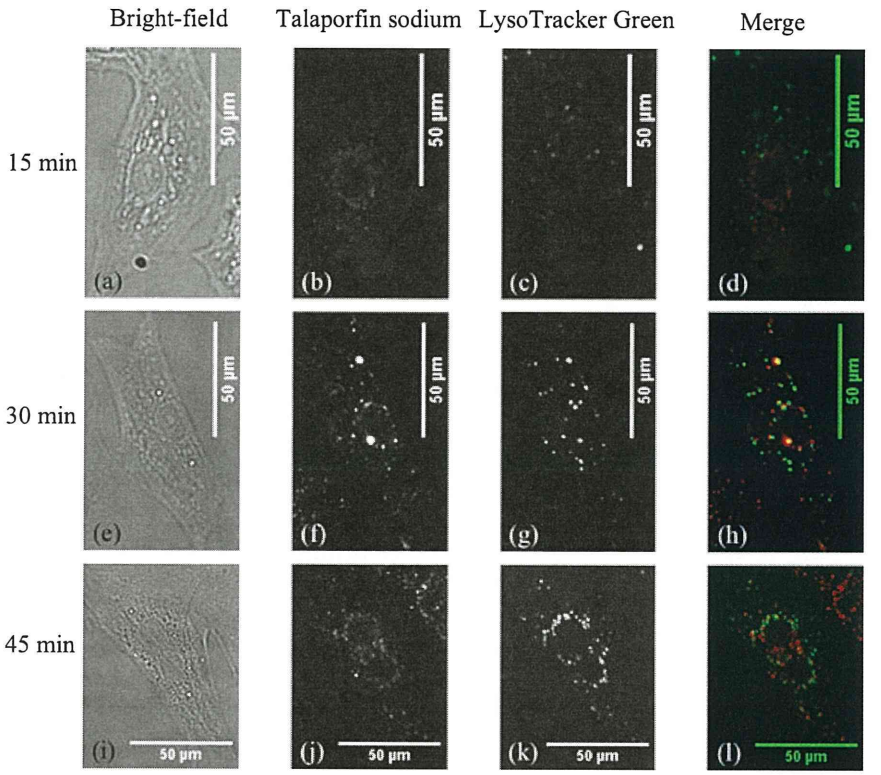

Figure 4. Intracellular talaporfin sodium distribution in rat myocardial cells. The cells were incubated in the medium containing talaporfin sodium (30 μg mL^{-1}) for 15 min [(a)–(d)], 30 min [(e)–(h)] and 45 min [(i)–(l)]. From left to right, bright-field image, talaporfin sodium fluorescence image, LysoTracker Green fluorescence image and the merged image of talaporfin sodium fluorescence and LysoTracker Green fluorescence.

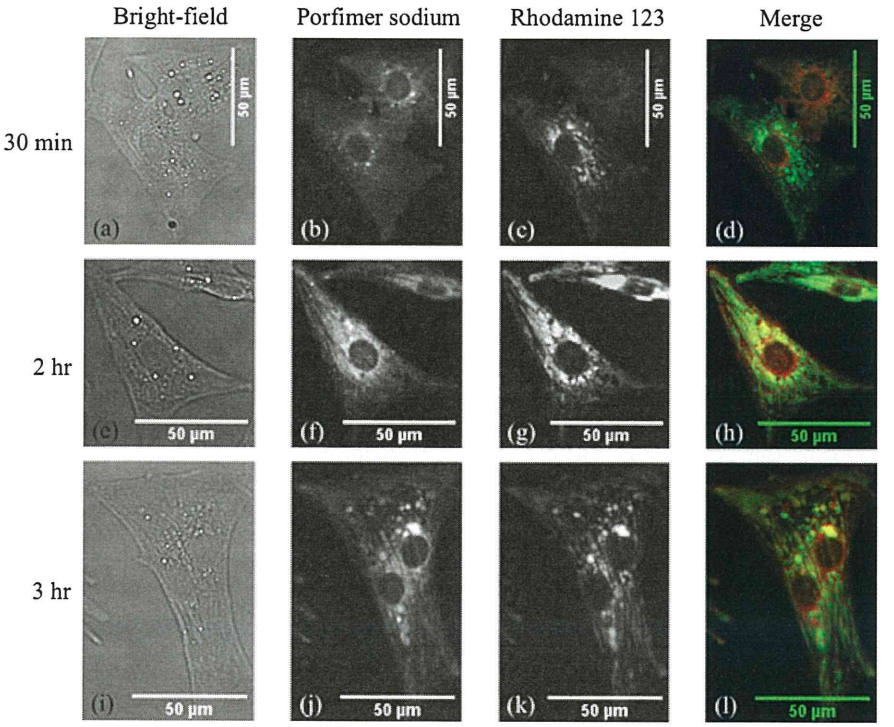

Figure 5. Intracellular porfimer sodium distribution in rat myocardial cells. Cells were incubated in the medium containing porfimer sodium (30 μg mL^{-1}) for 30 min [(a)–(d)], 2 h [(e)–(h)] and 3 h [(i)–(l)]. From left to right, bright-field image, porfimer sodium fluorescence image, Rhodamine 123 fluorescence image and the merged image of porfimer sodium fluorescence and Rhodamine 123 fluorescence.

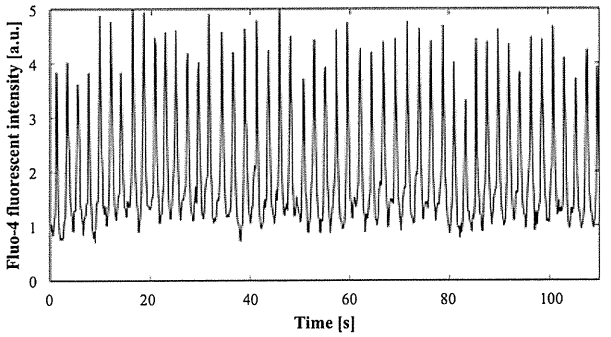

Figure 6. Changes in the control Fluo-4 fluorescence intensity without irradiation and with talaporfin sodium at 15 min loading.

almost uniform dim light of porfimer sodium fluorescence in all cells indicates that porfimer sodium was distributed in the cell membrane. The similarity between the fluorescence images of porfimer sodium and Rhodamine 123 was observed over 2–3 h of incubation (Fig. 5h,l). These results indicate that porfimer sodium distributed on the cell membrane at first for several tens of minutes of incubation and then relocalized to the mitochondria after several hours of further incubation.

Intracellular Ca^{2+} concentrations during the photosensitization reaction with talaporfin sodium or porfimer sodium

The acute subsecond response of intracellular free Ca^{2+} concentration ($[Ca^{2+}]_{in}$) of the myocardial cells to the exogenous photosensitization reaction with talaporfin sodium or porfimer sodium for a short period of photosensitizer incubation (15 min) was measured by using a confocal laser microscope. The time courses of the change in normal Fluo-4 fluorescence intensity in single myocardial cells are shown in Fig. 6, with the control condition being the presence of photosensitizer and the absence of photoactivation. The change in normal Fluo-4 fluorescence intensity of single myocardial cells was obtained as a control during the measurement period of 110 s. The well-known periodic change in intracellular Ca^{2+} concentration accompanied by excitation and contraction processes of myocardial cells, the so-called Ca^{2+} oscillation, was observed as the periodic increase and decrease in Fluo-4 fluorescence intensity (data not shown). The periodic change in Fluo-4 fluorescence intensity was not influenced by the addition of talaporfin sodium to the control (Fig. 6); the same result was obtained with porfimer sodium. There was almost no Fluo-4 photobleaching in this experimental setting during the measurement period. The laser used for Fluo-4 excitation was found to have less influence on the measurement of Fluo-4 fluorescence during the photosensitization reaction.

Figure 7a,b shows the change in Fluo-4 fluorescence intensity in single myocardial cells during the exogenous photosensitization reaction after the short period of incubation with talaporfin sodium (Fig. 7a) and porfimer sodium (Fig. 7b). A similar temporal pattern in the recorded change in Fluo-4 fluorescence intensity between both photosensitizers was observed when the photosensitizer was mainly located outside the cells. Soon after the start of irradiation, the amplitude of the periodic oscillation in the Fluo-4 fluorescence intensity

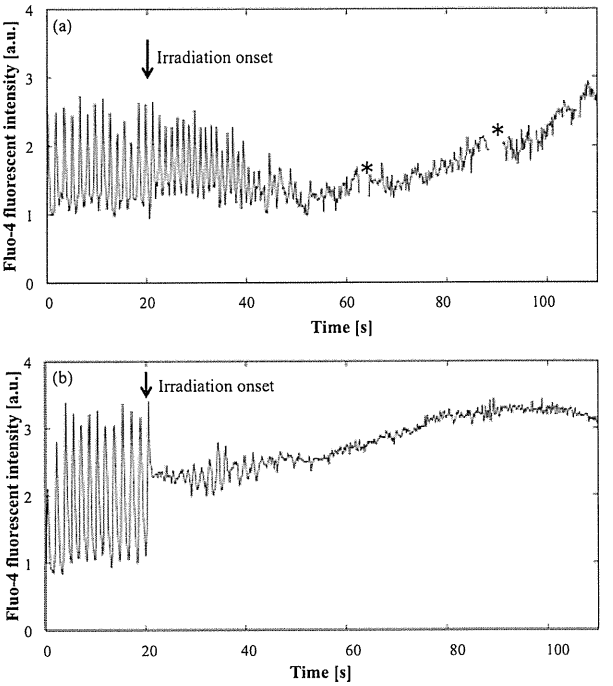

Figure 7. Changes in Fluo-4 fluorescence intensity during the exogenous photosensitization reaction after a short period of incubation with (a) talaporfin sodium and (b) porfimer sodium. The asterisks shown in the graph indicate the break for the focus adjustment.

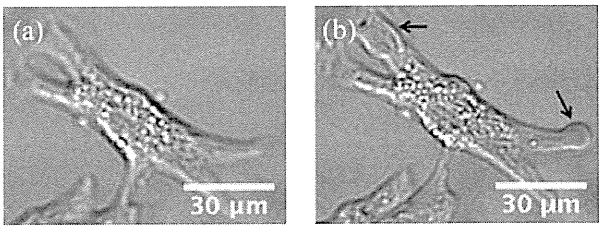

Figure 8. Morphological change (a) before and (b) 5 min after the photosensitization reaction with talaporfin sodium in a certain cell. The arrows shown in (b) indicate bleb formation.

disappeared within a few seconds. A subsequent irradiation induced a gradual increase in $[Ca^{2+}]_{in}$, which eventually exceed the maximum value in the normal oscillation. A drastic morphology change after the photosensitization reaction for the short period of incubation with talaporfin sodium, such as bleb formation, was observed on the surface of the myocardial cells without visible damage to the nuclei (Fig. 8), which was also observed in the reaction with porfimer sodium. However, there were differences in the extent of temporal response of the Fluo-4 fluorescence intensity to the photosensitization reaction between the photosensitizers. The time required for the oscillation amplitude to disappear was longer in the reaction with talaporfin sodium than that with porfimer sodium. A gentle slope in the temporal Fluo-4 fluorescence intensity change was obtained with talaporfin sodium.

In contrast, the photosensitization reaction with the photosensitizers distributed in the intracellular compartment showed a difference in the temporal tendency of the electrophysiological

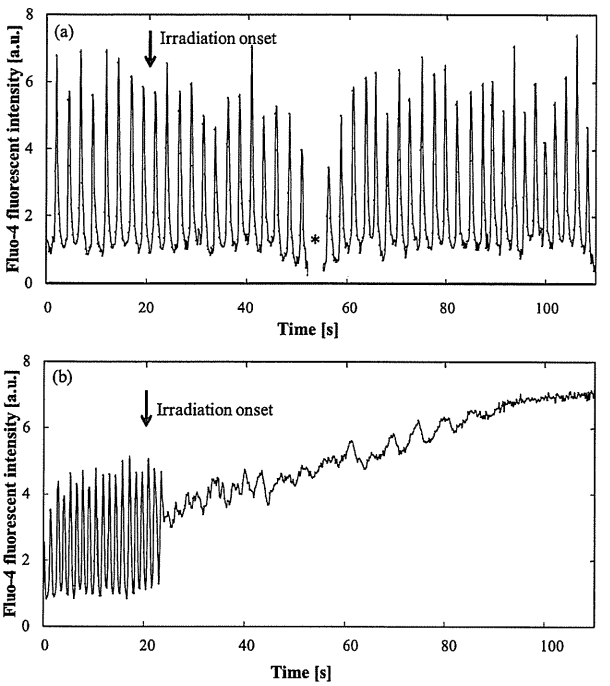

Figure 9. Changes in Fluo-4 fluorescence intensity during photosensitization reaction after a long period of incubation with (a) talaporfin sodium and (b) porfimer sodium. The asterisks shown in the graph indicate the break for the focus adjustment.

response between talaporfin sodium and porfimer sodium (Fig. 9a,b). Little change in the periodic oscillation of fluorescence intensity was observed with the photosensitization reaction in the long period of incubation with talaporfin sodium (Fig. 9a), indicating that the damage in the intracellular compartment, especially in lysosomes, might cause almost no acute effect on the electrophysiological cellular function. On the other hand, the photosensitization reaction in the long period of incubation with porfimer sodium induced the same response as in the short period of the photosensitizer incubation (Fig. 9b).

DISCUSSION

The subsecond intracellular calcium responses of rat myocardial cells to the photosensitization reaction for a short period of photosensitizer incubation showed similar temporal tendencies between both photosensitizers, talaporfin sodium and porfimer sodium (Fig. 7). The temporal characteristics of the Fluo-4 fluorescence intensity triggered by the photosensitization reaction could be divided into two phases: the first phase was the disappearance of Ca^{2+} oscillation, called the "phase I acute response," and the second phase was the gradual increase in $[Ca^{2+}]_{in}$, called the "phase II slow response." The regular spike showing normal activity of myocardial cells obtained before irradiation disappeared within the first several tens of seconds after the onset of photoactivation. This acute response might be caused by ion channel dysfunction because no microscopically significant cell morphological change was observed. After the disappearance of automaticity, there was a brief period of relatively constant level of Fluo-4 fluorescence

Table 1. The experimentally obtained decay time of the Ca^{2+} oscillation amplitude and average rate of change in $[Ca^{2+}]_{in}$ in various conditions.

	Talaporfin sodium		Porfimer sodium	
	Short period incubation	Long period incubation	Short period incubation	Long period incubation
Decay time of the Ca^{2+} oscillation amplitude (s)	11	-*	9.9	6.8
Average rate of change in $[Ca^{2+}]_{in}$ (nM s^{-1})	20.1	-*	44.5	82.9

*In the condition of long period of incubation with talaporfin sodium, there was almost no cellular response in $[Ca^{2+}]_{in}$ to the photosensitization reaction during the measurement period up to 200 s, so that the decay time and the average rate of $[Ca^{2+}]_{in}$ change defined as above definitions is not calculated.

intensity, followed by a gradual increase in Fluo-4 fluorescence intensity as the phase II slow response occurs. The elevation of the Fluo-4 fluorescence intensity in phase II is possibly induced by the Ca^{2+} influx due to the difference in Ca^{2+} concentration between inside and outside the cell. The Ca^{2+} influx and cell morphological changes such as bleb formation indicate that the photosensitization reaction in the short period of incubation might cause cell membrane damage, mostly micropore formation on the surface of the cell membrane.

To compare the early electrophysiological cellular response to the photosensitization reaction between the photosensitizers and between their distributions, the temporal characteristic of the change in intracellular Ca^{2+} concentration with the photosensitization reaction was examined in both the phase I acute response and the phase II slow response. We focused on one parameter in each phase. The first one in the phase I acute response is "decay time of the Ca^{2+} oscillation amplitude," which is defined as the time required for the oscillation amplitude in the Fluo-4 fluorescence intensity to decrease to 1/e of the pre-irradiation average value after the onset of the irradiation. The oscillation amplitude in the fluorescence intensity was defined as the difference between the maximum and minimum fluorescence intensities during the oscillation period obtained before the onset of irradiation. The oscillation amplitude decreased with time during the photosensitization reaction. The decay times of the oscillation amplitude in the three conditions, talaporfin sodium with a short period of incubation and porfimer sodium with a short/long period of incubation, are shown in Table 1. The decay time was longer in the photosensitization reaction with talaporfin sodium than that with porfimer sodium.

The second parameter is "average rate of change in $[Ca^{2+}]_{in}$" in the phase II slow response. After the oscillation disappearance followed by a brief period of relatively constant level in $[Ca^{2+}]_{in}$, then $[Ca^{2+}]_{in}$ began to increase with time. We define "average rate of change in $[Ca^{2+}]_{in}$" during about 20 s after the initiation of the $[Ca^{2+}]_{in}$ increase. To obtain the average rate of change in $[Ca^{2+}]_{in}$, the estimated intracellular Ca^{2+} concentration was calculated from the measured Fluo-4 fluorescence intensity in the range of the normal oscillation amplitude using the following equation (33).

$$[Ca^{2+}]_{in} = K_d \frac{F - F_{min}}{F_{max} - F} \quad (1)$$

where K_d is the dissociation constant of Fluo-4 reported to be 345 nM (32,34), F_{min} is the Fluo-4 fluorescence intensity in the absence of Ca^{2+}, F_{max} is the fluorescence intensity in saturated Ca^{2+} and F is the fluorescence intensity in intermediate Ca^{2+} levels. We assume that F_{min} is zero to calculate the intracellular Ca^{2+} concentration from Eq (1). The fluorescence intensity is normalized by the minimum value of the oscillation intensity before the irradiation onset, where $[Ca^{2+}]_{in}$ is assumed to be 100 nM (35). The average rate of change in $[Ca^{2+}]_{in}$ was obtained from the changes in $[Ca^{2+}]_{in}$ during the photosensitization reaction calculated using Eq (1). We assume that these gradual increases in $[Ca^{2+}]_{in}$ several tens of seconds after the initiation of $[Ca^{2+}]_{in}$ increase might be caused by the micropores formed on the cell membrane in the early stage of the photosensitization reaction and then by the Ca^{2+} influx through the micropores (13). The amount of the photosensitizer and oxygen might be restricted by the limited volume of our experimental setup; thus, oxygen might be possibly exhausted during the early stage of the photosensitization reaction. The initial oxygen concentration in the medium might correspond to 220 μM in the air-saturated solution at 25°C. The oxygen concentration of the photosensitizer solution might have suddenly decreased at the onset of the photosensitization reaction. Several observation of the exhaustion of oxygen during photosensitization reaction has been reported. For example, our research group has reported that oxygen concentration was decreased to 40% of the initial value after the photosensitization reaction with 6.0 μg mL^{-1} talaporfin sodium solution in the condition when the fluence was 1 J cm^{-2} and fluence rate was 200 mW cm^{-2} with a red diode laser (CW, λ = 670 nm) (29). We assume that a certain number of micropores might be formed in the photosensitization reaction with a limited amount of O_2 and then Ca^{2+} influx through the micropores might occur due to the difference in intracellular and extracellular Ca^{2+} concentrations. Table 1 shows the experimentally obtained average rate of change in $[Ca^{2+}]_{in}$ in three conditions: in the short period of incubation with talaporfin sodium and in the short/long period of incubation with porfimer sodium. The photosensitization reaction in the short period of incubation with porfimer sodium is found to induce twice as high average rate of change in $[Ca^{2+}]_{in}$ as with talaporfin sodium.

The shorter decay time of the Ca^{2+} oscillation amplitude (Table 1) and the higher average rate of change in $[Ca^{2+}]_{in}$ (Table 1) were obtained in the photosensitization reaction with porfimer sodium. We think that the parameter in phase I acute response, decay time of the Ca^{2+} oscillation amplitude, indicate the extent of the damage in cellular electrophysiological function such as ion channel malfunction and the other parameter in phase II slow response, average rate of change in $[Ca^{2+}]_{in}$, indicate the extent of the damage in cell membrane such as micropore formation. The results (Table 1) indicate that the earlier cellular response to the photosensitization reaction and the higher efficiency in membrane damage might be obtained with porfimer sodium than with talaporfin sodium. In our experimental condition, the molar energy of absorption per unit volume per unit time was higher with talaporfin sodium (2.8×10^3 J s^{-1} M^{-1} cm^{-3}) than with porfimer sodium (3.4×10^2 J s^{-1} M^{-1} cm^{-3}). Talaporfin sodium has been reported to have a larger triplet quantum yield than porfimer sodium (36), while the triplet state quenching rate is almost the same between the two photosensitizers: 1.3×10^9 M^{-1} s^{-1} for talaporfin sodium (37) and $1.4–1.8 \times 10^9$ M^{-1} s^{-1} for porfimer sodium (38–40). The singlet oxygen quantum yield in talaporfin sodium, 0.77 (37), is larger than that in HPD, 0.06–0.63 (38,41). Despite the higher singlet oxygen quantum yield and the higher molar energy of absorption in the photosensitization reaction with talaporfin sodium, our experimental results indicate that the slower response rate and lower efficiency in micropore formation might be affected by another factor, which might be the photosensitizer location. The photocytotoxic process depends on the distance between the photosensitizer and target cell or subcellular compartment due to the short diffusion path of the singlet oxygen during the lifetime (< 4 μs) in aqueous medium (42). In our experimental condition of short or long period of incubation with porfimer sodium, the lipophilic porfimer sodium might be located on and/or inside the cell membrane (Fig. 5). Lipophilic porphyrins have been reported to generate $^1O_2$ within the membrane bilayer in photoactivation, which might cause membrane protein damage, resulting in electric depolarization, increased permeability, membrane rupture and cell lysis (43–45). The intrinsic lifetime of $^1O_2$ has been reported to be relatively long (13–35 μs) in the lipid bilayer (46,47). Moreover, the membrane-bound porfimer sodium might cause lipid peroxidation effectively in type I reactions (48). In our experimental condition of long period of incubation, a large number of porfimer sodium molecules might be located between the lipid bilayer; thus, the porfimer sodium binding to cell membrane bilayer could induce a more effective micropore formation than that in the short period of incubation. On the other hand, the hydrophilic talaporfin sodium could not bind to the cell membrane; thus, its distance from the cell membrane might be longer than that of porfimer sodium. The singlet oxygen generated from the photoactivation of talaporfin sodium might interact with the cell membrane within an activation length. The activation length might be a diffusion radius of singlet oxygen during the lifetime, reported to be < 220 nm in aqueous solution (49). In our experimental condition for a short period of incubation with talaporfin sodium, the generated singlet oxygen, which might exist within the activation distance from the cell membrane, could cause micropore formation. Despite the long distance from the cell membrane, the higher amounts of singlet oxygen generated in the photosensitization reaction with talaporfin sodium might cause the same level of photocytotoxicity as with porfimer sodium. No electrical responses were observed in the condition of long period of incubation (Fig. 9a). Since talaporfin sodium was localized to the subcellular compartment, especially in the lysosome (Fig. 4), the singlet oxygen might be generated inside the lysosome. The activation path length of the singlet oxygen in the cell has been reported to be 10–20 nm (50,51). The singlet oxygen generated inside the lysosome might cause focal damage of the lysosome, resulting to apoptotic cell death.

In this study, we found that exogenous photosensitization reactions for a short period of photosensitizer incubation induce acute electrophysiological cellular responses and cell membrane damage with similar temporal tendencies between two photosensitizers; talaporfin sodium and porfimer sodium.

We also found that the photocytotoxic process differs between the two photosensitizers, with the main difference being the distance between the photosensitizers and their target (i.e. the cell membrane). The lipophilic porfimer sodium might cause direct membrane damage with small amounts of generated singlet oxygen, while the hydrophilic talaporfin sodium might cause the same level of damage to the cell membrane with large amounts of generated singlet oxygen.

Acknowledgements—This study was partially supported by the Supporting Program for Creating University Ventures (#1904) of the Japan Science and Technology Agency and by Research Fellowships of the Japan Society for the Promotion of Science for Young Scientists.

REFERENCES

1. Dougherty, T. J., C. J. Gomer, B. W. Henderson, G. Jori, D. Kessel, M. Korbelik, J. Moan and Q. Peng (1998) Photodynamic therapy (Review). *J. Natl Cancer Inst.* **90**, 889–905.
2. Schuitmaker, J. J., P. Baas, H. L. L. M. van Leengoed, F. W. van der Meulen, W. M. Star and N. van Zandwijk (1996) Photodynamic therapy: A promising new modality for the treatment of cancer. *J. Photochem. Photobiol. B, Biol.* **34**, 3–12.
3. Dougherty, T. J. (1993) Photodynamic therapy. *Photochem. Photobiol.* **58**, 895–900.
4. Oleinick, N. L., R. L. Morris and I. Belichenko (2002) The role of apoptosis in response to photodynamic therapy: What, where, why, and how. *Photochem. Photobiol. Sci.* **1**, 1–21.
5. Moore, J. V., C. M. L. West and C. Whitehurst (1997) The biology of photodynamic therapy. *Phys. Med. Biol.* **42**, 913–935.
6. Buytaert, E., M. Dewaele and P. Agostinis (2007) Molecular effectors of multiple cell death pathways initiated by photodynamic therapy. *Biochim. Biophys. Acta* **1776**, 86–107.
7. Spikes, J. D. and J. C. Bommer (1993) Photobleaching of mono-L-aspartyl chlorin e6 (NPe6): A candidate sensitizer for the photodynamic therapy of tumors. *Photochem. Photobiol.* **58**, 346–350.
8. Delinger, M. (1996) Apoptosis or necrosis following Photofrin® photosensitization: Influence of the incubation protocol. *Photochem. Photobiol.* **64**, 182–187.
9. Kessel, D., Y. Luo, Y. Deng and C. K. Chang (1997) The role of subcellular localization in initiation of apoptosis by photodynamic therapy. *Photochem. Photobiol.* **65**, 422–426.
10. Kessel, D., M. Castelli and J. Reiners Jr. (2002) What are the targets of photodynamic therapy? *Proc. SPIE* **4612**, 122–127.
11. Stark, G. (2005) Functional consequences of oxidative membrane damage. *J. Membr. Biol.* **205**, 1–16.
12. Zhou, Z., H. Yang and Z. Zhang (2003) Role of calcium in phototoxicity of 2-butylamino-2-demethoxy-hypocrellin A to human gastric cancer MGC-803 cells. *Biochim. Biophys. Acta* **1593**, 191–200.
13. Specht, K.G. and M. A. J. Rodgers (1991) Plasma membrane depolarization and calcium influx during cell injury by photodynamic action. *Biochim. Biophys. Acta* **1070**, 60–68.
14. Hubmer, A., A. Hermann, K. Uberreigler and B. Krammer (1996) Role of calcium in photodynamically induced cell damage of human fibroblasts. *Photochem. Photobiol.* **64**, 211–215.
15. Zong, W. X. and C. B. Thompson (2006) Necrotic death as a cell fate. *Genes Dev.* **20**, 1–15.
16. Bers, D. M. (2002) Cardiac excitation–contraction coupling. *Nature* **415**, 198–205.
17. Douplik, A., A. A. Stratonnikov, V. B. Loschchenov, V. S. Lebedeva, V. M. Derkacheva, A. Vitkin, V. D. Rumyanceva, S. G. Kusmin, A. F. Mironov and E. A. Luk'Yanets (2000) Study of photodynamic reactions in human blood. *J. Biomed. Opt.* **5**, 338–349.
18. Tarr, M., A. Frolov and D. P. Valenzeno (2001) Photosensitization-induced calcium overload in cardiac cells: Direct link to membrane permeabilization and calcium influx. *Photochem. Photobiol.* **72**, 418–424.
19. Ito, A., S. Hosokawa, S. Miyoshi, K. Soejima, S. Ogawa and T. Arai (2010) The myocardial electrical blockade induced by photosensitization reaction. *IEEE Trans. Biomed. Eng.* **57**, 488–495.
20. Penning, L. C., M. H. Rasch, E. Ben-Hur, T. M. A. R. Dubbelman, A. C. Havelaar, J. Van der Zee and J. Van Steveninck (1992) A role for transient increase of cytoplasmic free calcium in cell rescue after photodynamic treatment, *Biochim. Biophys. Acta* **1107**, 255–260.
21. Pass, H. I. (1993) Photodynamic therapy in oncology: Mechanisms and clinical use. *J. Natl Cancer Inst.* **85**, 443–456.
22. Hsieh, Y.J., C. C. Wu, C. J. Chang and J. S. Yu (2003) Subcellular localization of Photofrin® determines the death phenotype of human epidermoid carcinoma A431 cells triggered by photodynamic therapy: When plasma membranes are the main targets. *J. Cell. Physiol.* **194**, 363–375.
23. Aizawa, K., T. Okunaka, T. Ohtani, H. Kawabe, Y. Yasunaka, S. O'Hata, N. Ohtomo, K. Nishimiya, C. Konaka, H. Kato, Y. Hayata and T. Saito (1987) Localization of mono-L-aspartyl chlorin e6 (NPe6) in mouse tissues. *Photochem. Photobiol.* **46**, 789–793.
24. Kato, H., K. Furukawa, M. Sato, T. Okunaka, Y. Kusunoki, M. Kawahara, M. Fukuoka, T. Miyazawa, T. Yana, K. Matsui, T. Shiraishi and H. Horinouchi (2003) Phase II clinical study of photodynamic therapy using mono-image-aspartyl chlorin e6 and diode laser for early superficial squamous cell carcinoma of the lung. *Lung Cancer* **42**, 103–111.
25. Chan, A. L., M. Juarez, R. Allen, W. Volz and T. Albertson (2005) Pharmacokinetics and clinical effects of mono-l-aspartyl chlorin e6 (NPe6) photodynamic therapy in adult patients with primary or secondary cancer of the skin and mucosal surfaces. *Photodermatol. Photoimmunol. Photomed.* **21**, 72–78.
26. Roberts, W. G. and M. W. Berns (1989) In vitro photosensitization I. Cellular uptake and subcellular localization of mono-L-aspartyl chlorin e6, chloro-aluminum sulfonated phthalocyanine, and photofrin II. *Lasers Surg. Med.* **9**, 90–101.
27. Roberts, W. G., L. H. L. Liaw and M. W. Berns (1989) In vitro photosensitization II. An electron microscopy study of cellular destruction with mono-l-aspartyl chlorin e6 and photofrin II. *Lasers Surg. Med.* **9**, 102–108.
28. Reiners Jr, J. J., J. A. Caruso, P. Mathieu, B. Chelladurai, X. M. Yin and D. Kessel (2002) Release of cytochrome c and activation of pro-caspase-9 following lysosomal photodamage involves bid cleavage. *Cell Death Differ.* **9**, 934–944.
29. Ohmori, S., S. Hakomori, T. Tsukahara and T. Arai (2007) A comparative study between pulsed and continuous wave irradiation for Talaporfin sodium mediated photosensitization in solution, in-vitro and in-vivo. *Rev. Laser Eng.* **35**, 180–186.
30. Caruso, J. A., P. A. Mathieu and J. J. Reiners Jr. (2005) Sphingomyelins suppress the targeted disruption of lysosomes/endosomes by the photosensitizer NPe6 during photodynamic therapy. *Biochem. J.* **392**, 325–334.
31. Seguchi, H., M. Ritter, M. Shizukushi, H. Ishida, G. Chokoh, H. Nakazawa, K. W. Spitzer and W. H. Barry (2005) Propagation of Ca^{2+} release in cardiac myocytes: Role of mitochondria. *Cell Calcium* **38**, 1–9.
32. Gee, K. R., K. A. Brown, W. N. U. Chen, J. Bishop-Stewart, D. Gray and I. Johnson (2000) Chemical and physiological characterization of fluo-4 Ca^{2+} indicator dyes. *Cell Calcium* **27**, 97–106.
33. Minta, A., J. P. Kao and R. Y. Tsien (1989) Fluorescent indicators for cytosolic calcium based on rhodamine and fluorescein chromophores. *J. Biol. Chem.* **264**, 8171–8178.
34. Haugland, R. P. (1996) *Handbook of Fluorescent Probes and Research Chemicals*. 6th edn, 505 pp. Molecular Probes Inc., Eugene, OR.
35. Berridge, M. J., P. Lipp and M. D. Bootman (2000) The versatility and universality of calcium signaling. *Nat. Rev. Mol. Cell Biol.* **1**, 11–21.
36. Ohmori, S. and T. Arai (2006) In vitro behavior of Porfimer sodium and Talaporfin sodium with high intensity pulsed irradiation. *Lasers Med. Sci.* **21**, 213–223.
37. Spikes, J. D. and J. C. Bommer (1993) Photosensitizing properties of mono-L-aspartyl chlorin e6 (NPe6): a candidate sensitizer for

the photodynamic therapy of tumors. *J. Photochem. Photobiol. B, Biol.* **17**, 135–143.
38. Reddi, E., M. A. Rodgers and G. Jori (1984) Photophysical and photosensitizing properties of hematoporphyrin bound with human serum albumin. *Prog. Clin. Boil. Res.* **170**, 373–379.
39. Sterenborg, H. and M. J. C. Gemert (1996) Photodynamic therapy with pulsed light sources: A theoretical analysis. *Phys. Med. Biol.* **41**, 835–849.
40. Bonnett, R., C. Lambert, E. J. Land, P. A. Scourides, R. S. Sinclair and T. G. Truscott (1983) The triplet and radical species of haematoporphyrin and some of its derivatives. *Photochem. Photobiol.* **38**, 1–8.
41. Blum, A. and L. I. Grossweiner (1985) Singlet oxygen generation by hematoporphyrin IX, uroporphyrin I and hematoporphyrin derivative at 546 nm in phosphate buffer and in the presence of egg phosphatidylcholine liposomes. *Photochem. Photobiol.* **41**, 27–32.
42. Merkel, P. B. and D. R. Kearns (1972) Radiationless decay of singlet molecular oxygen in solution. Experimental and theoretical study of electronic-to-vibrational energy transfer. *J. Am. Chem. Soc.* **94**, 7244–7253.
43. Ehrenberg, B., E. Gross, Y. Nitzan and Z. Malik (1993) Electric depolarization of photosensitized cells: Lipid vs. protein alterations. *Biochim. Biophys. Acta* **1151**, 257–264.
44. Kessel, D. (1984) Hematoporphyrin and HPD: photophysics, photochemistry and phototherapy. *Photochem. Photobiol.* **39**, 851–859.
45. Dubbelman, T., A. De Goeij and J. Van Steveninck (1978) Protoporphyrin-sensitized photodynamic modification of proteins in isolated human red blood cell membranes. *Photochem. Photobiol.* **28**, 197–204.
46. Ehrenberg, B., J. L. Anderson and C. S. Foote (1998) Kinetics and yield of singlet oxygen photosensitized by hypericin in organic and biological media. *Photochem. Photobiol.* **68**, 135–140.
47. Henderson, B. W. and T. J. Dougherty (1992) How dose photodynamic therapy work? *Photochem. Photobiol.* **55**, 145–157.
48. Athar, M., H. Mukhtar and D. R. Bickers (1998) Differential role of reactive oxygen intermediates in photofrin-I- and photofrin-II-mediated photoenhancement of lipid peroxidation in epidermal microsomal membranes. *J. Invest. Dermatol.* **90**, 652–657.
49. Redmond, R. W. and I. E. Kochevar (2006) Spatially resolved cellular responses to singlet oxygen. *Photochem. Photobiol.* **82**, 1178–1186.
50. Moan, J. and K. Berg (1991) The photodegradation of porphyrins in cells can be used to estimate the lifetime of singlet oxygen. *Photochem. Photobiol.* **53**, 549–553.
51. Moan, J. (1990) On the diffusion length of singlet oxygen in cells and tissues. *J. Photochem. Photobiol. B, Biol.* **6**, 343–347.

Safety and efficacy of pericardial endoscopy by percutaneous subxyphoid approach in swine heart in vivo

Takehiro Kimura, MD,[a] Shunichiro Miyoshi, MD, PhD,[a] Seiji Takatsuki, MD, PhD,[a] Kojiro Tanimoto, MD, PhD,[a] Kotaro Fukumoto, MD, PhD,[a] Kyoko Soejima, MD, PhD,[b] and Keiichi Fukuda, MD, PhD[a]

Objective: A nonsurgical approach from the epicardial surface is useful for various cardiac interventions, such as positioning of the left ventricular lead for cardiac resynchronization therapy and epicardial ablation. Stem cell delivery on the epicardial surface can be considered in the future if good quality of visualization can be obtained. However, because the pericardial space is limited, hemodynamic conditions may deteriorate with pericardial endoscopy. Therefore, the feasibility and efficacy of pericardial endoscopy were examined by using ready-made endoscopes.

Methods: Anesthetized swines (26–61 kg; n = 6) were used for the experiment. Electrocardiogram, femoral artery blood pressure, and oxygen saturation by pulse oximetry were continuously monitored during the procedures. Guided by the fluoroscopy, sheaths were advanced to the pericardial space using the modified Seldinger technique from the subxyphoid space.

Results: After insertion of an endoscope with a maximum diameter of 6.9 mm, hemodynamic parameters were stable during the procedure with atropine. Stable and acceptable endoscopic images were obtained. Minor operations can be performed with pericardial endoscopic-guided laparoscopic forceps with no complications.

Conclusions: The endoscopic pericardial procedure is effective and feasible. This procedure can increase the possibility and efficacy of nonsurgical treatment for cardiac diseases. (J Thorac Cardiovasc Surg 2011;142:181-90)

Video clip is available online.

Recent progress in minimally invasive therapy has dramatically changed the treatment of heart disease. Percutaneous transluminal approaches (eg, coronary angioplasty[1]; catheter ablation[2,3]; pacemaker, implantable cardioverter defibrillator, and cardiac resynchronization therapy[4]; and percutaneous heart valve replacement[5]) have provided significant therapeutic benefit to patients with a minimal burden. However, it is still difficult to reach the epicardial targets by the transluminal approach. Minimally invasive epicardial approaches may aid epicardial biopsy, implantation of left ventricular epicardial pacing lead for cardiac resynchronization therapy, and ablation for epicardial arrhythmic substrate. Furthermore, such approaches are also applicable for transplantation of stem cells into the myocardium. Although significant progress in research for cardiac stem cells has been made, research for optimization of the transplantation procedures is sparse. Compared with catheter-based transluminal stem cell transplantation,[6] epicardial transplantation poses less risk for infusion of stem cells into the bloodstream and systemic dissemination and microembolization of overflowed stem cells.[7,8] Pericardial endoscopy is also applicable to direct genetic transfection of the gene to the local myocardium, so-called gene therapy.[9]

Pericardiocentesis using the Seldinger maneuver from the subxyphoid to the pericardial space without obvious pericardial effusions is safe[10] and allows the epicardial target to be reached with minimal invasion.[11,12] However, it is difficult to perform the operation within the pericardial space because of numerous obstacles: the coronary vessels, adipose tissue, lung, and phrenic nerves. Therefore, endoscopic guidance is required for the operation. Epicardial biopsy,[13,14] epicardial ablation,[15] pulmonary vein isolation,[16] and implantable cardioverter defibrillator lead placement[17] using pericardial endoscopy have been reported, but risk of injury to arteries, organs, and nerves still remains. The relation among the diameter of the endoscope, material of the sheath, and hemodynamic parameters has not been extensively described. Epicardial inflammation as a chronic effect should be further evaluated. Techniques to obtain a more refined view for critical procedures are not well developed.

Therefore, we evaluated the safety of this procedure, not only for short time periods to assess hemodynamic changes

From Cardiology,[a] Keio University School of Medicine, Tokyo, Japan; and Cardiology,[b] St. Marianna University School of Medicine, Kawasaki, Japan.

Experiments were partially supported by the Japanese Society for Promotion of Science, Grant-in-Aid for Scientific Research, the Ministry of Health, Labor, and Welfare of Japan, and the Suntory Fund for Advanced Cardiac Therapeutics, Keio University School of Medicine. Part of the work was performed at the Keio Research Laboratory Center for Integrated Medical Research.

Disclosures: Authors have nothing to disclose with regard to commercial support.

Received for publication Aug 1, 2010; revisions received Sept 5, 2010; accepted for publication Sept 11, 2010; available ahead of print Nov 12, 2010.

Address for reprints: Takehiro Kimura, MD, 35 Shinanomachi Shinjuku-ku Tokyo, Japan 160-8582, Cardiology, Keio University School of Medicine (E-mail: veritas@bp.iij4u.or.jp).

0022-5223/$36.00

doi:10.1016/j.jtcvs.2010.09.050

Abbreviation and Acronym
CCD = charge-coupled device

but also for longer periods to assess chronic complications, including infections, chronic pericarditis, and other life-threatening complications. Among various ready-made endoscopes, adequate types for pericardial endoscopy were selected. To identify the anatomy of the heart, we defined the basic method to steer the endoscope and stabilize the view.

MATERIALS AND METHODS

Surgical Procedure

All experimental protocols were approved by the institutional ethical committee. Studies were performed in 6 mongrel swine weighing 26 to 61 kg. After nitrous oxide inhalation, swine were intubated and ventilated with room air by the constant-volume cycled respirator (Harvard Apparatus model 607; Harvard Appatatus, Hoilliston, Mass) and anesthetized with 1.5% to 2% isoflurane. A fluid-filled cannula was placed in the left carotid artery and connected to the transducer to monitor arterial blood pressure. A great cervical vein cannula was used to infuse normal saline at a rate of 100 to 200 mL/h to replace spontaneous fluid losses and to inject drugs. Electrocardiogram and pulse oxymetry were continuously monitored.

Mechanical irritation of the pericardium may cause Bezold–Jarisch (vagal) reflex and bradycardia that can result in significant deterioration of hemodynamics; therefore, immediately before the pericardiocentesis, 1 mg of atropine was administered to suppress the vagal reflex and an additional 0.5 mg of atropine was administered when the heart rate decreased to less than 70 beats/min. After local anesthesia, an 18G epidural needle connected to a 10-mL syringe filled with contrast material was inserted from the subxyphoid toward the heart shadow under x-ray fluoroscopic guidance.[18] After puncture of the pericardial membrane, the guide wire (outer diameter = 0.81 mm) was inserted into the pericardial space, and the catheter sheath was inserted along the guide wire to the pericardial space. We used 6 types of sheaths. The size, stiffness, shape, and material of each sheath are shown in Figure 1. Sheaths were selected in accordance with the diameter of the endoscope. Six ready-made endoscopes (Olympus Medical Systems Corp, Tokyo, Japan) were used. The model number, visual angle, direction of lens, size, device ports, optical image system, and features of the endoscopes are shown in Figure 2. The endoscopes are advanced through the variety of sheaths, checking the effects of hemodynamic data, controllability, and quality of the view. We tried to maintain a clear view by regulating the amount of air and saline insufflations through the working port of the endoscope. Measured vital signs, fluoroscopic images, and endoscopic images were analyzed and evaluated after each experiment. To assess chronic effects, animals were kept alive for 2 weeks and then inspected for evidence of injuries to pericardium, lungs, and other organs.

RESULTS

Effect of Endoscope and Sheath Size on Hemodynamic Parameters

The performance of the endoscope increases as a function of the diameter of the endoscope; however, the hemodynamics may deteriorate. Thus, the adequate diameter of the endoscope with acceptable visual images without significantly changing the hemodynamics should be determined. Representative hemodynamic data during pericardial endoscopy are shown in Figure 3. The endoscope with the largest diameter (6.9 mm in ES5) did not cause significant deterioration of hemodynamic parameters; thus, the endoscope with a diameter less than 6.9 mm is acceptable.

To obtain a clear image, design of the optomechanical device is important. Mounting a charge-coupled device (CCD) camera on the tip of the endoscope to connect directly to the objective lens significantly improved image quality (Figure 4, *D, F*). However, this is difficult to do with a thinner endoscope because of limitations on the miniaturization of the CCD camera. Therefore, the CCD camera was mounted

No	ID(F)	Model	Material	Stiffness	Shape	Check valve	Image
SH1	10	radifocus introducer-IIH	polypropylene	soft	curved	tight	
SH2	15	hand made	polypropylene	soft	straight	tight	
SH3	21	hand made	polytetra-fluoroethylene	floppy	floppy	tight	
SH4	18	capiox percutaneous catheter kit	polypropylene	hard	curved	none	
SH5	16.5	TOLOCKER Ø 5.5mm	stainless	solid	straight	loose	
SH6	33	TOLOCKER Ø 11mm	stainless	solid	straight	loose	

FIGURE 1. List of the sheaths used. Internal diameter in French, model name, material, stiffness, shape of the tip, durability of the check valve, and an image of the sheath (*white scale bars* = 5 cm). *ID,* Internal diameter; *F,* French.

No	Model	Visual angle(°)	Direction of lens(°)	Ø OD(mm)	Device port (Ømm)	Adequate sheath	CCD on the Tip	Purpose or usage	Image	Performance
ES1	URF-P5	90	0	2.9	1.2	SH1	×	Designed for pyelo-urine tract		poor
ES2	BF-XP160F	90	0	3.25	1.2	SH1 SH2 SH5	×	Designed for tracho-bronchial tract		poor
ES3	BF-MP160F	120	0	5.0	2.0	SH2 SH5	×	Designed for tracho-bronchial tract		moderate
ES4	IPLEX FX IM8420	120	90	4.0	non	SH2 SH3 SH4	○	Designed for industrial usage, I.e., to check internal surface of pipes. Robotic controller attached		good
ES5	BF TYPE UC160F-OL8	80	35	6.9	2.0	SH3 SH4 SH6	×	Designed for tracho-bronchial tract, with ultrasonic imaging system		well
ES6	GIF-XP150N	120	0	5.5	2.0	SH3 SH4 SH5	○	Designed for trans-nasal gastro-intestine camera		good

FIGURE 2. List of the endoscopes used. Models of the endoscope, visual angle, direction of lens (angle along the longitudinal axis), outer diameter, inner diameter of utility port, adequate sheath, whether CCD camera is mounted on the tip or not, features of the endoscope, images of the endoscope (*scale bars* = 5 mm), and the performance of the endoscope in the pericardial space. *CCD,* Charge-coupled device; *OD,* outer diameter.

on the body of the thin endoscope and connected to the objective lens by a bundle of flexible optic fibers, which significantly improved image quality (Figure 4, *A–C, E*). Because the thickest endoscope (outer diameter = 6.9 mm) was hemodynamically tolerable, we concluded that mounting the CCD on the endoscope tip was adequate for pericardial endoscopy. Taking these results into account, we selected ES4 and ES6 as adequate for a pericardial endoscope.

The selection of the sheath was more important. To insert a large endoscope into a pericardial space, sheaths with a larger diameter are required, but ready-made larger sheaths are uncommon (SH1, SH5, SH6) and most of them are solid (SH5, SH6). Solid sheaths were unstable in positioning, and use of SH6 sometimes caused significant deterioration of hemodynamic parameters. Therefore, after insertion of the endoscope, withdrawal of the sheath was required to stabilize hemodynamic parameters (Figure 3, *A*). Accordingly, we prepared our handmade flexible sheath with a larger diameter (SH2, SH3, SH4), which did not cause a significant change in hemodynamic parameters (Figure 3, *B*). A check valve on the sheath was also important to maintain the volume of air in the pericardial space. The SH3 exhibited the best performance.

Clear Visualization

Our first achievement was to establish the method to obtain a clear view of the pericardial space by endoscopy. Expansion of the pericardial space by air enables us to maintain a distance from the camera to the heart surface, which is necessary for a clear view. An equal volume of saline was injected in some experiments, but a good image was not obtained and there was significant deterioration of hemodynamic parameters (Figure 3, *B*). Therefore, we decided to inject air to expand the pericardial space.

A larger amount of air infusion provides better vision, but on the other hand it may deteriorate hemodynamic parameters by inhibiting diastolic function of the ventricles. Injection of 100 to 200 mL of gas into the pericardial space caused no hemodynamic changes (±5 mm Hg) and allowed a stable view. In addition, resulting decreases in systolic blood pressure were less than 10 mm Hg, which is almost tolerable.

Orientation of the View

Determination of orientation of the view is important for an endoscopic-guided operation. Because of strong motion artifacts in the visual field, x-ray fluoroscopic guidance is essential to determine orientation of the tip of the endoscope. Furthermore, recognition of several landmarks of the heart can also help in understanding orientation. Infusion of 10 to 20 mL of saline and 50 to 100 mL of air into the pericardial space gives us a clear view of fluid levels. The fluid level is an important compass for horizontal direction of the visual field. Landmarks (Figure 5) in the visual

ET/BS

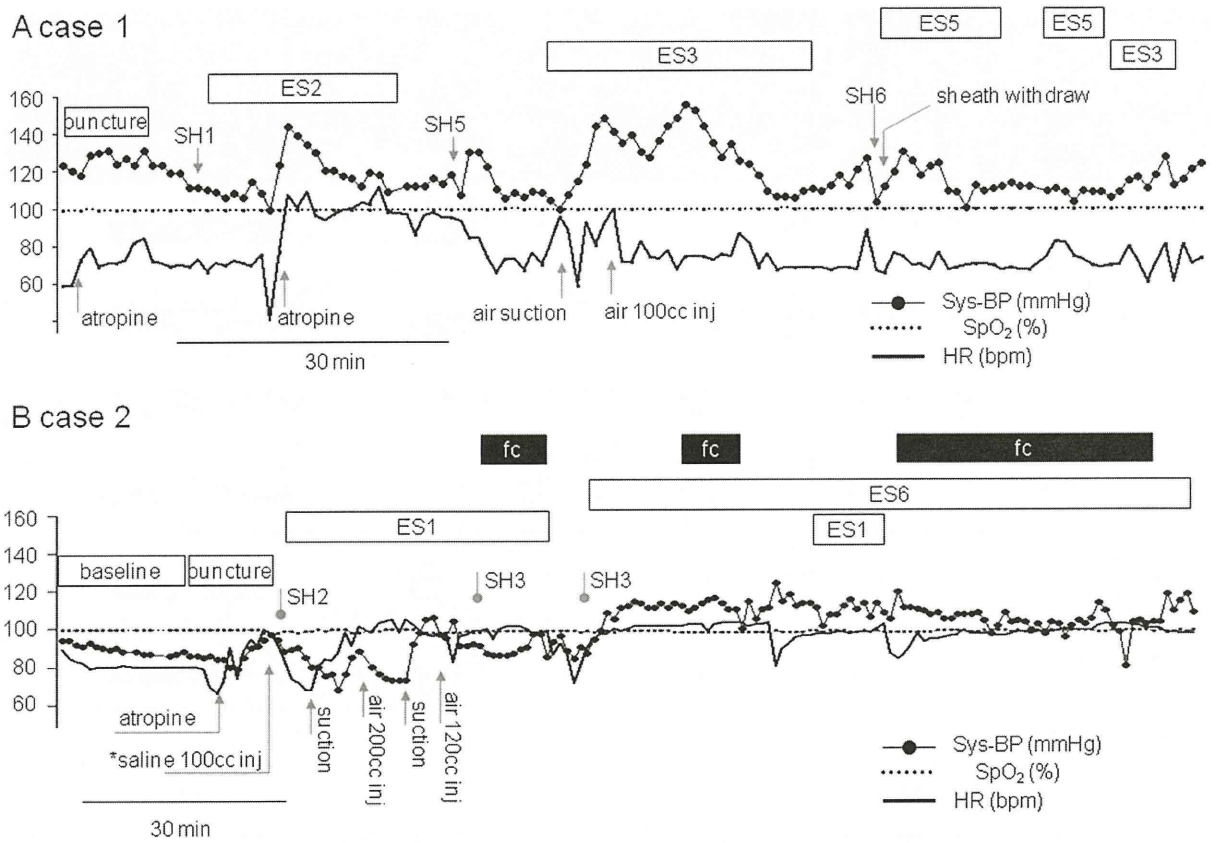

FIGURE 3. Systolic blood pressure, pulse oxymetry, and heart rate as a function of time during procedures of representative cases. *Upper white bars* in the graphs denote period of endoscope insertion, and *black bars* denote insertion of laparoscopic forceps. *Upper gray arrows* denote the time of insertion of each sheath, and *lower gray arrows* denote the timing of administration of atropine, suction, and injection of air/saline into the pericardial space. Hemodynamic parameters during procedure are well within tolerable limits. *Sys-BP,* Systolic blood pressure; *SpO_2,* pulse oxymetry; *HR,* heart rate; *ES,* endoscope; *fc,* forceps; *SH,* sheath.

field also help us to recognize the position of the tip of the endoscope. Left and right atrial appendages are clear landmarks (Figure 5, *A, C, M, P, Q, S, T, U*). Other heart landmarks, that is, the aortic root (Figure 5, *K*), pulmonary veins (Figure 5, *G, N*), superior vena cava (Figure 5, *E*), and coronary arteries (Figure 4, *A–F*; Figure 5, *R*), also give us a clue to define the orientation. Adjacent organs—the lung, diaphragmatic membrane (Figure 5, *I, W*), and puncture site (Figure 5, *V*)—can be good landmarks.

Control of Endoscopes

It is an advantage to understand the movement of the endoscope to stabilize the tip of the device at the exact location. After the modified Seldinger technique, the anteroapical portion of the pericardium was penetrated by sheaths. By advancing and retracting the endoscope, the tip of the endoscope simply moved forward and backward along the anterior interventricular groove. In this manner, the endoscope was straight, the x-ray showed an "I-shape" configuration, and the heart was observed as in an upward-viewing manner (apex to base direction, Figure 6, *F*). As the endoscope was advanced, the left anterior descending coronary artery (Figure 4, *A, E, F*), left atrial appendage (Figure 4, *E*; Figure 5, *A, M, S, T*), and aortic root were observed (Figure 5, *K*). By bending the endoscopic tip toward the right side, the outflow tract and right ventricle (Figure 5, *O*) were observed; by bending toward the left, the left pulmonary veins could be observed (Figure 5, *G*). However, this view was unstable; because the support (backup) of the shaft was only a shallow interventricular groove, the tip was easily dislodged. Therefore, another endoscopic control is required to observe the whole heart.

When we gently advanced the endoscope in the I-shape configuration under a fluoroscopic guide (Figure 6, *A, F*), the tip was trapped at the position along the roof (cranial end, Figure 6, *B*) of the pericardial space, between the right ventricular outflow tract and the left atrial appendage. At this position, if we rotated the shaft clockwise and advanced the endoscope with maximally bending the tip

ET/BS

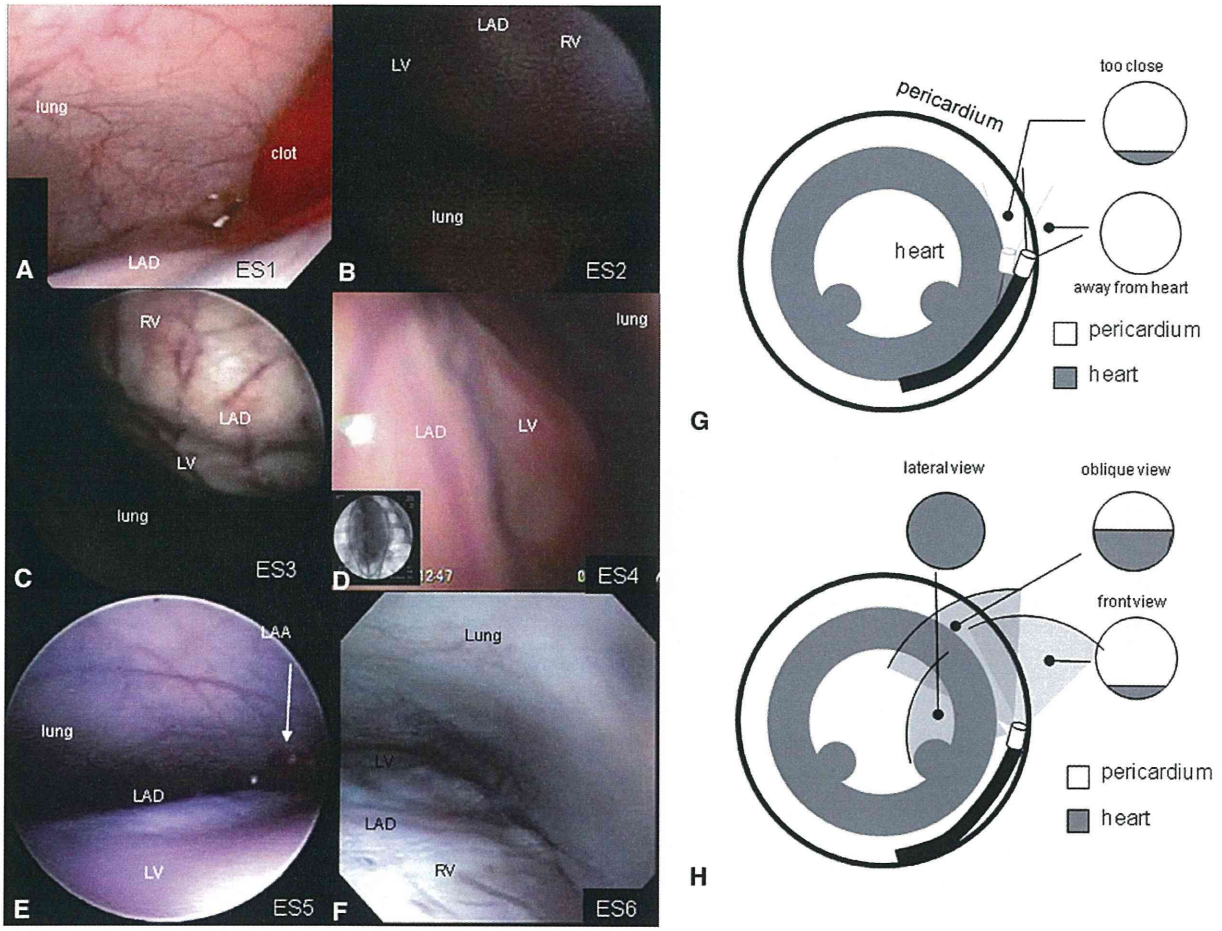

FIGURE 4. A–F, Representative images of left anterior descending artery observed by each endoscope (denoted right bottom, number corresponding to it in Figure 1). It is difficult to front-view the endoscope with a narrow visual angle (A, B). Images of the endoscope without mounting the CCD on the tip (C, E) are fuzzy. Images of the endoscope with the CCD on the tip (D, F) are vivid. G, H, Schematic diagram of spatial configuration of endoscope in the pericardial space and its visual field. G, If the head of the front-view endoscope is directed to the heart surface, the objective lens gets too close to the heart surface. On the other hand, if the endoscope is tipped away from the heart surface, the visual field of the endoscope also tips away from the heart. H, The relation between the visual field and the direction of the objective lens. *LAD,* Left anterior descending artery; *LV,* left ventricle; *ES,* endoscope; *RV,* right ventricle.

(Figure 6, *C*), the tip of the endoscope could be advanced into the right side of the pericardial space. The middle shaft was turned around at the caudal roof of the pericardium, resulting in a so-called inverted U-shape right-side configuration (Figure 6, *D, E, G, H*), allowing the heart to be observed as in a downward-viewing manner (base to apex direction). On the other hand, if we rotated the shaft counterclockwise and advanced the endoscope, the tip of the endoscope could go through the left side of the heart, and a so-called inverted U-shape left-side configuration could be achieved. By use of the inverted U-shape configurations, we could observe every portion of the epicardium (Figure 6, *H*; Video 1).

To effectively control pericardial endoscopy, it is important to take into account the position of backup of the shaft and fulcrum at the point of bending. First, the shaft was fixed at the puncture point of the pericardium. In the I-shape configuration, the shaft was moderately backed up by the anterior interventricular groove, the rotation of the shaft did not help steering devices, and the fulcrum point of bending was only the epicardium. Therefore, it was difficult to keep a distance between the objective lens and the epicardial surface (Figure 4, *G*), resulting in loss of focus and significant halation (Figure 5, *X*). However, when the tip was advanced and bent, the visual field was directed toward the pericardium and kept a distance from the epicardial surface (Figure 4, *G*). Finally, in the inverted U-shape configuration, the middle of the shaft was strongly backed up by the whole pericardium and we could steer the devices by rotating the shaft. This configuration enabled us to keep an appropriate distance from the epicardial surface (Figure 4, *H*; Video 2).

ET/BS

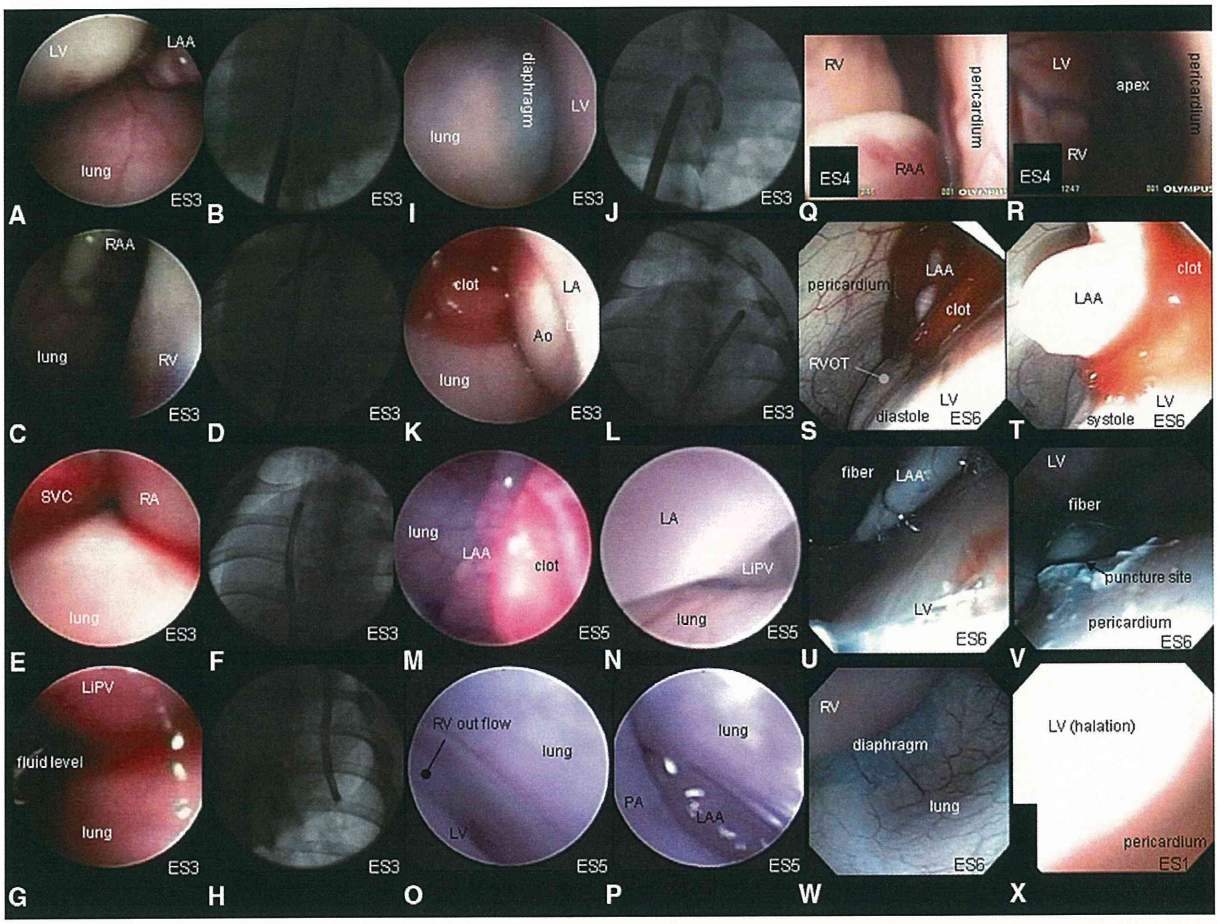

FIGURE 5. Representative images obtained by endoscopy and fluoroscopy. Endoscopic images (A, C, E, G, I, K) obtained by ES3 and corresponding fluoroscopic images (B, D, F, H, J, L, respectively). A, Left atrial appendage and lateral wall of left ventricle. C, Right atrial appendage and lateral wall of right ventricle. E, Superior vena cava and right atrium. G, Left inferior pulmonary vein. I, Pericardium at the diaphragm looks pale compared with pericardium at the lungs. K, Left ventricular outflow tracts. Aortic root and left atrium can be observed. M–P, Endoscopic images obtained by ES5. Left atrial appendage (M, P), left inferior pulmonary vein (N), and pulmonary artery outflow tract (O, P). Q, R, Endoscopic images obtained by ES4. Right atrial appendage (Q), right ventricle (Q, R), and ventricular apex (*apex*, R). S–W, Endoscopic images obtained by ES6. S, T, Sequential image showing dynamic motion of left atrial appendage. U, Left atrial appendage and body of fiber itself. V, Pericardial puncture site and the body of fiber itself. W, Pericardium at the diaphragm. The quality of the images obtained by ES6 is superior to that obtained by ES3. X, Image obtained by ES1. By using the front-view ES with a narrow visual angle, it is difficult to observe the heart surface without significant halation. *Ao,* Aortic; *ES,* endoscopy; *LA,* left atrium; *LAA,* left atrial appendage; *LiPV,* left inferior pulmonary vein; *LV,* left ventricle; *PA,* pulmonary artery; *RA,* right atrium; *RAA,* right atrial appendage; *RV,* right ventricle; *S,* diastole; *SVC,* superior vena cava; *T,* systole.

Feasibility of Minor Surgery

We tested the feasibility of endoscope-guided small operations in the pericardial space. To simulate transplantation of stem cells into the myocardium from the epicardium, we injected Indian ink into the epicardium via endoscope. A 1-mL syringe with 0.2 mL of Indian ink was connected to a 22G needle for endoscopy (NA-201SX-4022; Olympus, Tokyo, Japan). The needle tip was insulated by external Teflon tubing to avoid injury to the coronary vessels. The needle was attached to the surface of the left ventricular free wall via a utility port (Figure 7, *A*). After positioning of the tip, the internal needle was protruded into the myocardium, and then Indian ink was injected without severe hemorrhage (Figure 7, *B*). By protruding the external tube, the objective lens and surface of the heart were stabilized to significantly reduce strong motion artifacts, and adequate working distance was achieved (Figure 7, *C*).

Rigid laparoscopic forceps are essential for endoscope-guided surgery; however, such rigid forceps may compress the heart and deteriorate hemodynamic parameters. Therefore, a flexible endoscope (ES6) and rigid laparoscopic forceps (Figure 7, *E*) were inserted simultaneously to perform

ET/BS

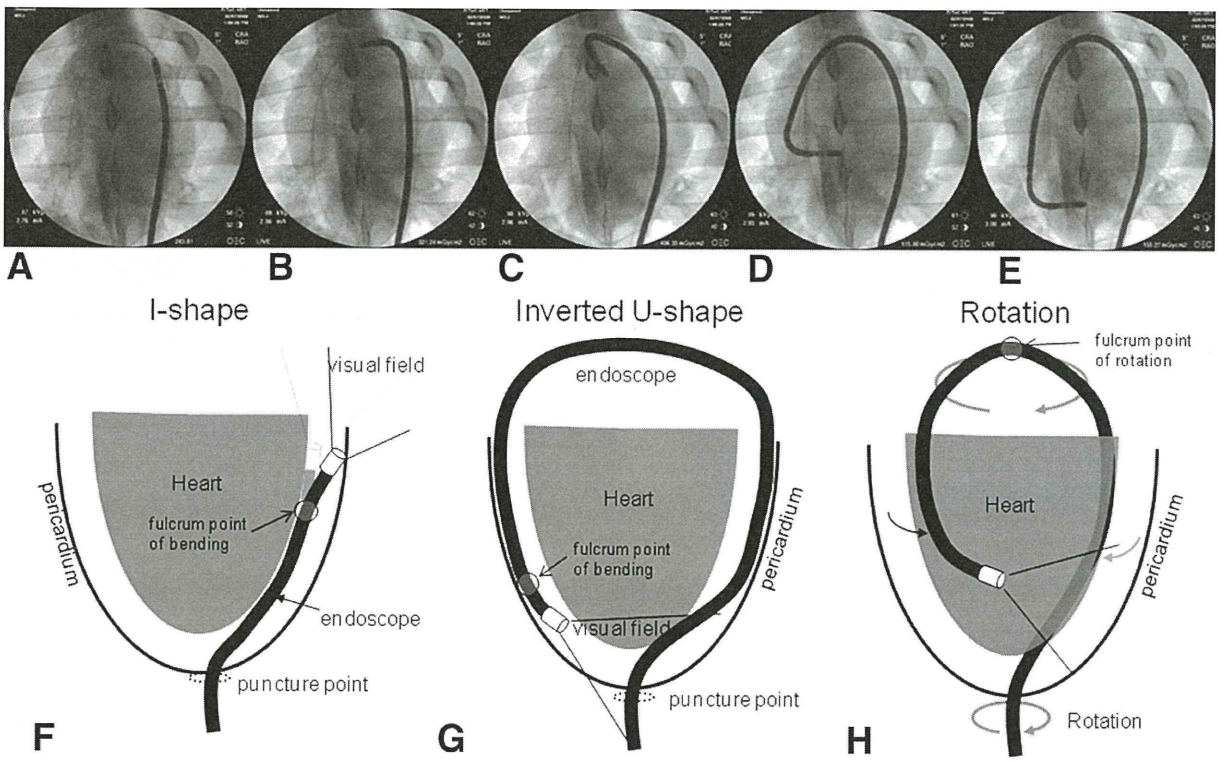

FIGURE 6. A–E, Sequential fluoroscopic images during changing I-shape configuration to inverted U-shape configuration. See details in text. F–H, Schematic diagram of I-shape configuration, inverted U-shape configuration of pericardial endoscope, and how to steer the tip of the endoscope in the pericardial space.

minor surgery (Figure 7, *F–H*). A needle-type pacing electrode (Figure 7, *I*) was transplanted into the left ventricular free wall by use of ES6 (Figure 7, *F–H*). Transplantation was successfully performed without significant hemodynamic change (Figure 7, *J–L*; Video 2).

Complications

Because pericardial endoscopy is the leading minimally invasive technique, the safety of this procedure is our main concern. In the process of puncture by the Seldinger technique, there were no complications, such as hemorrhages, pneumothorax, perforation of left ventricle, or other injuries. During the whole procedure, we could handle the devices in and out numerous times with no changes in blood pressure, pulse oxymetry data, or heart rate (Figure 3) for more than 1 hour. The injection of more than 200 mL of air into the pericardial space suppresses blood pressure by 5 to 10 mm Hg, but blood pressure recovers immediately by removing air from the space via endoscopic utility port.

In terms of chronic phases, pericardial inflammation was evaluated 2 weeks after the operations. There were no macroscopic injuries, coronary stenosis by coronary angiogram, hemorrhages, or adhesion of pericardium (Figure 7, *D*).

DISCUSSION

Selection of Best Endoscope

Because the first priority for pericardial endoscopy is a clear image, an endoscope with a CCD camera on the tip is essential. In popular endoscopes, the objective lens is usually positioned toward an anterior direction (forward-view, ES1, ES2, ES3, ES6). When the endoscope is inserted into the pericardial space, a shaft of the endoscope usually fits along the curve of the epicardial surface, but the objective lens faces toward a tangent direction to the epicardial surface and away from the surface of the heart (Figure 4, *G*). It is reasonable to imagine that positioning the objective lens in a 30- to 60-degree interior oblique direction may be another option (Figure 4, *H*). From an optomechanical point of view, it is difficult to position the lens and CCD complex on the thin tip of endoscopes, although a lens with a 90-degree direction (lateral-view, ES4) can be achieved. Also, so-called fish-eye lenses or wider visual angle lenses (ES3, ES4, ES6) enable observation of the heart surface, even if the distance between the heart and the device is not sufficient.

A diameter less than 6.9 mm with a soft shaft is acceptable, and utility port is necessary for controlling air and devices. Among the ready-made endoscopes, the ES6 showed

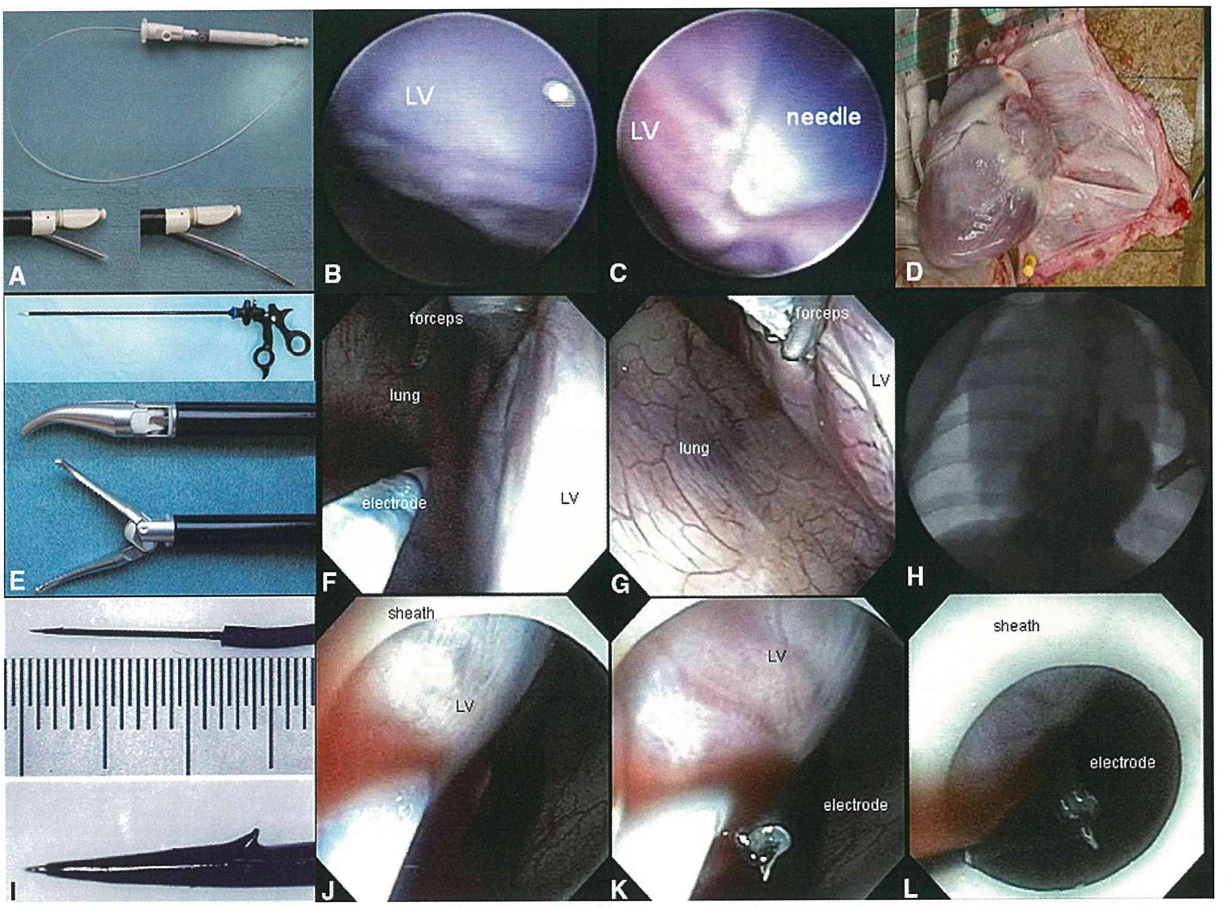

FIGURE 7. A–C, Indian ink was injected into the left ventricular epicardium with a needle. B, Immediately after injection of Indian ink, there was no active bleeding. D, Two weeks after the pericardial endoscopy, there was no coronary injury and no marked adhesion of pericardium. E, Laparoscopic forceps used. *F, G,* Endoscopic (ES6) images during implantation of pacing lead (I) in the left ventricular muscle by using laparoscopic forceps and fluoroscopic images during procedure (H). Implanted pacemaker lead immediately after the implantation (J–L). *LV,* Left ventricle.

the best performance. The ES4 also showed good performance, but there is no utility port for intervention.

Selection of Best Sheath

A certain length of the sheath should be positioned in the pericardial space to obtain back-up support for intervention. By advancing the sheaths, the direction of the sheath is usually perpendicular to the heart surface. A solid sheath causes significant compression of the heart surface and deterioration of hemodynamic parameters. Thus, a floppy sheath is suitable for pericardial endoscopy. Furthermore, to maintain the amount of air within the pericardial space, a check valve at the top of the sheath is essential. Taking this into account, we selected SH4 as the best sheath for pericardial endoscopy.

Stabilization of Motion Artifacts

Stabilization of strong motion artifacts is important. Keeping a distance from the heart surface by use of the inverted U-shape configuration can help stabilize the visual field. Gentle compression of the heart by a rigid manipulator, such as sheaths and laparoscopic forceps, can also stabilize the heartbeat.

Optimization of the Tools

Although we demonstrated the feasibility of the pericardial endoscope by ready-made endoscopes, optimization of the tools should be required. The ES6 is almost acceptable as a pericardial endoscope if we have well-designed forceps for interventions through the utility port. On the other hand, further optimization of the manipulator should be done for pericardial interventions, such as an optimized tool for a cell-delivery system, epicardial pacemaker implantation, and curving of the tip to fit along the heart curvature. The design for the sheath should also be optimized. The optimal material, stiffness, and curve of the sheath remain to be elucidated.

ET/BS

Limitations

Before application for human use, the pericardial endoscopic system should be optimized, and further experiments should be done in other conditions. For example, we did not try the system on an animal with heart failure; therefore, the feasibility of the procedure in the patient with severe heart failure is still undetermined.

We performed the experiment under general anesthesia with respirator support, but for humans this procedure could be performed with local anesthesia. However, in patients with congenital pericardial defect, of which there is a prevalence of 0.0001%[19] to 0.044%,[20] infusion of the gas may cause pneumothorax, so respirator support should be required in such cases.

During this procedure, coincidental occurrence of ventricular fibrillation should be carefully monitored. If this occurs, immediate suction of the gas should be required to perform successful external defibrillation.

It was difficult to observe the posterior surface of the heart because of the limited space between the posterior wall of left atrium and the spine. If the target is the posterior portion of the heart, a lateral position of the patient may gain space and avoid puddling at the focus area. Further experiments should be done for safer procedures.

Clinical Applications

The future of this new technique relies on optimizing its use in humans. Previous studies have demonstrated the effective use of the pericardial approach in the human body, and the device itself is already well known and used clinically. Therefore, there are no obstacles to human application. This method enables us to reach epicardial areas and deep into the myocardium to focus on ablation and implantable cardioverter/defibrillator lead placement in a minimally invasive way. In the present study, we infused air into the pericardial space. However, there is less chance of causing air embolism and significant mediastinal emphysema with carbon dioxide compared with air. For clinical application, infusion of carbon dioxide gas is considered to be safer in this system.

Moreover, in cardiac stem cell therapy, there is no standard method of stem cell transplantation. Transplantation via coronary vessels may not deliver the cells to the appropriate location in the heart tissue, may occlude coronary vessels, and may generate additional myocardial infarctions.[7] Direct injection into the myocardium from an endocardial site via a needle devised on the tip of a catheter using an electroanatomic mapping system (NOGA System, Biosense Webster, Markham, ON, Canada)[6] is similar to the common catheter ablation procedure. Although the catheter procedure is safe and can be performed repeatedly, the injected cells may backflush into the left ventricular cavity via needle trajectory and disseminate into the systemic circulation, causing systemic microembolizations. From this point of view, injection of the cells from the epicardial surface is secure. However, open chest surgery is required to avoid coronary vessels. Pericardial endoscopy-guided cellular transplantation from the epicardial surface can be a major method for stem cell transplantation.

CONCLUSIONS

Our experiment has established a new and simple method for obtaining a clear view of the pericardial space with the use of pericardial endoscopy. The percutaneous subxyphoid approach using the Seldinger technique was useful and safe. An x-ray fluoroscopic guide was necessary to steer the endoscope in the pericardial space. We have shown short- and long-term safety with regard to hemodynamic changes, infections, and adhesion of pericardium. Pericardial endoscopy can introduce a new era of technology for cardiac surgeons and cardiac interventionists.

The authors thank Olympus Corporation for technical advice and Satoshi Ogawa, MD, PhD, and Toshiaki Satoh, MD, PhD, for medical advice.

References

1. Gruntzig AR, Senning A, Siegenthaler WE. Nonoperative dilatation of coronary-artery stenosis: percutaneous transluminal coronary angioplasty. *N Engl J Med.* 1979;301:61-8.
2. Gallagher JJ, Svenson RH, Kasell JH, German LD, Bardy GH, Broughton A, et al. Catheter technique for closed-chest ablation of the atrioventricular conduction system. *N Engl J Med.* 1982;306:194-200.
3. Scheinman MM, Morady F, Hess DS, Gonzalez R. Catheter-induced ablation of the atrioventricular junction to control refractory supraventricular arrhythmias. *JAMA.* 1982;248:851-5.
4. Abraham WT, Fisher WG, Smith AL, Delurgio DB, Leon AR, Loh E, et al. Cardiac resynchronization in chronic heart failure. *N Engl J Med.* 2002;346: 1845-53.
5. Cribier A, Eltchaninoff H, Bash A, Borenstein N, Tron C, Bauer F, et al. Percutaneous transcatheter implantation of an aortic valve prosthesis for calcific aortic stenosis: first human case description. *Circulation.* 2002; 106:3006-8.
6. Perin EC, Dohmann HF, Borojevic R, Silva SA, Sousa AL, Mesquita CT, et al. Transendocardial, autologous bone marrow cell transplantation for severe, chronic ischemic heart failure. *Circulation.* 2003; 107:2294-302.
7. Vulliet PR, Greeley M, Halloran SM, MacDonald KA, Kittleson MD. Intra-coronary arterial injection of mesenchymal stromal cells and microinfarction in dogs. *Lancet.* 2004;363:783-4.
8. Breitbach M, Bostani T, Roell W, Xia Y, Dewald O, Nygren JM, et al. Potential risks of bone marrow cell transplantation into infarcted hearts. *Blood.* 2007;110: 1362-9.
9. Kikuchi K, McDonald AD, Sasano T, Donahue JK. Targeted modification of atrial electrophysiology by homogeneous transmural atrial gene transfer. *Circulation.* 2005;111:264-70.
10. Ota T, Degani A, Zubiate B, Wolf A, Choset H, Schwartzman D, et al. Epicardial atrial ablation using a novel articulated robotic medical probe via a percutaneous subxiphoid approach. *Innovations Phila Pa.* 2006;1:335-40.
11. Soejima K, Couper G, Cooper JM, Sapp JL, Epstein LM, Stevenson WG. Subxiphoid surgical approach for epicardial catheter-based mapping and ablation in patients with prior cardiac surgery or difficult pericardial access. *Circulation.* 2004;110:1197-201.

12. Soejima K, Stevenson WG, Sapp JL, Selwyn AP, Couper G, Epstein LM. Endocardial and epicardial radiofrequency ablation of ventricular tachycardia associated with dilated cardiomyopathy: the importance of low-voltage scars. *J Am Coll Cardiol.* 2004;43:1834-42.
13. Maisch B, Bethge C, Drude L, Hufnagel G, Herzum M, Schonian U. Pericardioscopy and epicardial biopsy—new diagnostic tools in pericardial and perimyocardial disease. *Eur Heart J.* 1994;15(Suppl C):68-73.
14. Seferovic PM, Ristic AD, Maksimovic R, Tatic V, Ostojic M, Kanjuh V. Diagnostic value of pericardial biopsy: improvement with extensive sampling enabled by pericardioscopy. *Circulation.* 2003;107:978-83.
15. Nazarian S, Kantsevoy SV, Zviman MM, Matsen FA 3rd, Calkins H, Berger RD, et al. Feasibility of endoscopic guidance for nonsurgical transthoracic atrial and ventricular epicardial ablation. *Heart Rhythm.* 2008;5:1115-9.
16. Gerosa G, Bianco R, Buja G, di Marco F. Totally endoscopic robotic-guided pulmonary veins ablation: an alternative method for the treatment of atrial fibrillation. *Eur J Cardiothorac Surg.* 2004;26:450-2.
17. Zenati MA, Bonanomi G, Chin AK, Schwartzman D. Left heart pacing lead implantation using subxiphoid videopericardioscopy. *J Cardiovasc Electrophysiol.* 2003;14:949-53.
18. Spodick DH. The technique of pericardiocentesis. When to perform it and how to minimize complications. *J Crit Illn.* 1995;10:807-12.
19. Southworth H, Stevenson CS. Congenital defects of the pericardium. *Arch Intern Med.* 1938;223-40.
20. Van Son JA, Danielson GK, Schaff HV, Mullany CJ, Julsrud PR, Breen JF. Congenital partial and complete absence of the pericardium. *Mayo Clin Proc.* 1993; 68:743-7.

STEM CELLS®

STEM CELL TECHNOLOGY: EPIGENETICS, GENOMICS, PROTEOMICS, AND METABONOMICS

Treatment of Human Mesenchymal Stem Cells with Angiotensin Receptor Blocker Improved Efficiency of Cardiomyogenic Transdifferentiation and Improved Cardiac Function via Angiogenesis

YOHEI NUMASAWA,[a] TAKEHIRO KIMURA,[a] SHUNICHIRO MIYOSHI,[a] NOBUHIRO NISHIYAMA,[a] NAOKO HIDA,[a] HIROKO TSUJI,[a] HIKARU TSURUTA,[a] KAORU SEGAWA,[b] SATOSHI OGAWA,[a] AKIHIRO UMEZAWA[c]

[a]Department of Cardiology and [b]Department of Microbiology and Immunology, Keio University School of Medicine, Tokyo, Japan, [c]Department of Reproductive Biology and Pathology, National Research Institute for Child Health and Development, Tokyo, Japan

Key Words. Angiotensin • Bone marrow stromal cells • Transdifferentiation • Stem cell transplantation

ABSTRACT

To improve the modest efficacy of mesenchymal stem cell (MSC) transplantation, the treatment of human MSCs with angiotensin receptor blockers (ARBs) was investigated. MSCs were cultured with or without the medium containing 3 μmol/l of ARBs before cardiomyogenic induction. After cardiomyogenic induction in vitro, cardiomyogenic transdifferentiation efficiency (CTE) was calculated by immunocytochemistry using anticardiac troponin-I antibody. In the nude rat chronic myocardial infarction model, we injected MSCs pretreated with candesartan (A-BM; $n = 18$) or injected MSCs without pretreatment of candesartan (BM; $n = 25$), each having survived for 2 weeks. The left ventricular function, as measured by echocardiogram, was compared with cardiomyogenic transdifferentiation in vivo, as determined by immunohistochemistry. Pretreatment with ARBs significantly increased the CTE in vitro (10.1 ± 0.8 $n = 12$ vs. $4.6 \pm 0.3\%$ $n = 25$, $p < .05$). Transplantation of candesartan-pretreated MSCs significantly improved the change in left ventricular ejection fraction (BM; -7.2 ± 2.0 vs. A-BM; $3.3 \pm 2.3\%$). Immunohistochemistry revealed significant improvement of cardiomyogenic transdifferentiation in A-BM in vivo (BM; 0 ± 0 vs. A-BM; $0.014 \pm 0.006\%$). Transplantation of ARB-pretreated MSCs significantly improved cardiac function and can be a promising cardiac stem cell source from which to expect cardiomyogenesis. STEM CELLS *2011;29:1405–1414*

Disclosure of potential conflicts of interest is found at the end of this article.

INTRODUCTION

Regeneration therapies have attracted a great deal of medical attention. Various cellular resources such as embryonic stem cells [1], mesenchymal stem cells (MSCs) [2], mononuclear cells [3, 4], and endothelial progenitor cells (EPCs) [5] have been candidates for the regeneration therapies. The majority of cells derived from bone marrow (BM) consist of blood cells in various stages of differentiation; however, BM also contains, hematopoietic stem cells, EPCs, and MSCs. MSCs have characteristics of replication competence and multipotency [2, 6–8], as reported in numerous studies of MSCs.

Mesenchymal cells are classified as somatic stem cells and exist in BM stroma, dermis, skeletal muscle, uterine endometrial gland [9], umbilical cord blood [7, 10], placenta [11], amniotic membrane [6], etc. They are known to be capable of transdifferentiating into bone, cartilage, skeletal muscles, fats, ligaments, vascular endothelium, smooth muscle, and cardiomyocytes. Among the various mesenchymal cell sources, BM-derived MSCs (BM-MSCs) can be used in an autologous manner; therefore, there are no immunological problems in transplantations. However, in terms of cardiomyogenic transdifferentiation, the efficiency of human BM-MSCs is extremely low [8] in vitro, and efficiency of human BM-MSC transplantation is modest in in vivo [12, 13] and in clinical trials [14, 15]. The limited effect in clinical trials may be due to low angiogenic and paracrine effect of human BM-MSCs, low cardioprotective effect on host myocardium, and partially due to low cardiomyogenic transdifferentiation efficiency (CTE) [8]. We have previously shown that human mesenchymal cells derived from younger populations, that is,

Author contributions: Y.N., T.K., N.N., H. Tsuji, H. Tsuruta, and K.S.: conception and design, collection and assembly of data, final approval of manuscript; S.M.: conception and design, administrative support, collection and assembly of data, data analysis and interpretation, manuscript writing, final approval of manuscript; N.H.: conception and design, collection and assembly of data; S.O.: financial support, administrative support, final approval of manuscript; A.U.: financial support, administrative support, final approval of manuscript. Y.N. and T.K. contributed equally to this article.

Correspondence: Shunichiro Miyoshi, M.D., Ph.D., Keio University School of Medicine, 35-Shinanomachi, Shinjuku-ku, Tokyo 160-8582, Japan. Telephone: 81-3-3353-1211, ext. 61421; Fax: 81-3-5363-3875; e-mail: smiyoshi@cpnet.med.keio.ac.jp Received March 8, 2011; accepted for publication June 30, 2011; first published online in STEM CELLS *EXPRESS* July 13, 2011.
1066-5099/2009/$30.00/0 doi: 10.1002/stem.691